

DTIC FILE COPY

4

RADC-TR-88-269
In-House Report
November 1988



AD-A223 231

THE VALIDATION AND APPLICATION OF A BISTATIC TWO-SCALE OF SURFACE ROUGHNESS SCATTERING MODEL

Robert J. Papa and Margaret B. Woodworth

APPROVED FOR PUBLIC RELEASE; DISTRIBUTION UNLIMITED.

DTIC
UNCLASSIFIED
DATE 2 3 1990

co

ROME AIR DEVELOPMENT CENTER
Air Force Systems Command
Griffiss Air Force Base, NY 13441-5700

90 06 25 170

This report has been reviewed by the RADC Public Affairs Division (PA) and is releasable to the National Technical Information Service (NTIS). At NTIS it will be releasable to the general public, including foreign nations.

RADC-TR-88-269 has been reviewed and is approved for publication.

APPROVED:



J. LEON POIRIER
Chief, Applied Electromagnetics Division
Directorate of Electromagnetics

APPROVED:



JOHN K. SCHINDLER
Director of Electromagnetics

FOR THE COMMANDER:



JOHN A. RITZ
Directorate of Plans & Programs

If your address has changed or if you wish to be removed from the RADC mailing list, or if the addressee is no longer employed by your organization, please notify RADC (EECE) Hanscom AFB MA 01731-5000. This will assist us in maintaining a current mailing list.

Do not return copies of this report unless contractual obligations or notices on a specific document require that it be returned.

UNCLASSIFIED

SECURITY CLASSIFICATION OF THIS PAGE

REPORT DOCUMENTATION PAGE				Form Approved OMB No. 0704-0188	
1a. REPORT SECURITY CLASSIFICATION Unclassified		1b. RESTRICTIVE MARKINGS			
2a. SECURITY CLASSIFICATION AUTHORITY N/A		3. DISTRIBUTION / AVAILABILITY OF REPORT Approved for public release; Distribution unlimited			
2b. DECLASSIFICATION / DOWNGRADING SCHEDULE N/A					
4. PERFORMING ORGANIZATION REPORT NUMBER(S) RADC-TR-88-269		5. MONITORING ORGANIZATION REPORT NUMBER(S)			
6a. NAME OF PERFORMING ORGANIZATION Rome Air Development Center		6b. OFFICE SYMBOL (If applicable) RADC/EECE		7a. NAME OF MONITORING ORGANIZATION	
6c. ADDRESS (City, State, and ZIP Code) Hanscom AFB Massachusetts 01731-5000		7b. ADDRESS (City, State, and ZIP Code)			
8a. NAME OF FUNDING / SPONSORING ORGANIZATION		8b. OFFICE SYMBOL (If applicable)		9. PROCUREMENT INSTRUMENT IDENTIFICATION NUMBER	
8c. ADDRESS (City, State, and ZIP Code)		10. SOURCE OF FUNDING NUMBERS			
		PROGRAM ELEMENT NO. 61102F	PROJECT NO. 2305	TASK NO. J4	WORK UNIT ACCESSION NO. 09
11. TITLE (Include Security Classification) The Validation and Application of a Bistatic Two-Scale of Surface Roughness Scattering Model					
12. PERSONAL AUTHOR(S) Papa, R.J. and Woodworth, M.B.					
13a. TYPE OF REPORT Scientific Interim		13b. TIME COVERED FROM 1/3/88 TO 7/20/88		14. DATE OF REPORT (Year, Month, Day) 1988 November	
15. PAGE COUNT 52					
16. SUPPLEMENTARY NOTATION					
17. COSATI CODES			18. SUBJECT TERMS (Continue on reverse if necessary and identify by block number)		
FIELD	GROUP	SUB-GROUP	Radar Clutter Bistatic radar Diffuse scattering		
DET	17	09			
PHYSICIS	20	14			
19. ABSTRACT (Continue on reverse if necessary and identify by block number) Bistatic configurations are being considered in several modern surveillance radar concepts. This introduces new clutter and target scattering cross section representations as a result of the more complex geometry. In this report three bistatic clutter topics are addressed. First, a bistatic two-scale of roughness terrain scattering model is validated by comparison with data. Second, the contributions from each roughness level are evaluated as a function of the scattering angle regimes. Third, comparisons of monostatic and bistatic clutter cross section maps for a loam surface are made for a bistatic radar configuration. Results showed generally good agreement between model and data except at low grazing angles where problems arise for experimental cross section measurements and single scattering assumptions in the model. Examination of the individual component contribution shows distinct behavior patterns and regions of dominance. Finally, the clutter mapping shows that for the configuration studied the bistatic cross sections were always much larger than the corresponding monostatic values. (KR) ←					
20. DISTRIBUTION/AVAILABILITY OF ABSTRACT <input type="checkbox"/> UNCLASSIFIED/UNLIMITED <input checked="" type="checkbox"/> SAME AS RPT. <input type="checkbox"/> DTIC USERS			21. ABSTRACT SECURITY CLASSIFICATION Unclassified		
22a. NAME OF RESPONSIBLE INDIVIDUAL Robert J. Papa			22b. TELEPHONE (Include Area Code) (617) 377-3585		22c. OFFICE SYMBOL RADC/EECE

DD FORM 1473, JUN 86

Previous editions are obsolete.

SECURITY CLASSIFICATION OF THIS PAGE

UNCLASSIFIED

Contents

1. INTRODUCTION	1
2. MODEL VALIDATION	1
2.1 Theory	2
2.2 Data and Model Parameters	6
2.3 Comparisons of Model Results with Data	7
3. ASSESSMENT OF SURFACE ROUGHNESS CONTRIBUTIONS	14
4. BISTATIC AND MONOSTATIC CLUTTER MAPS	37
5. CONCLUSIONS	42
REFERENCES	45

Illustrations

1. Surveillance Geometries for a Bistatic System or a Monostatic System	3
2. RCS vs. ϕ_S for Loam	8
3. RCS vs. ϕ_S for Loam	9
4. RCS vs. ϕ_S for Loam	10
5. RCS vs. ϕ_S for Loam	11
6. RCS vs. ϕ_S for Loam	12
7. RCS vs. ϕ_S for Loam	13
8. RCS vs. θ_S for Sand	15
9. RCS vs. θ_S for Sand	16
10. RCS vs. θ_S for Sand	17
11. RCS vs. θ_S for Sand	18
12. RCS vs. ϕ_S for Loam	19
13. RCS vs. ϕ_S for Loam	20
14. RCS vs. ϕ_S for Loam	21
15. RCS vs. ϕ_S for Loam	22
16. RCS vs. ϕ_S for Loam	23

Illustrations

17.	RCS vs. ϕ_S for Loam	24
18.	RCS vs. ϕ_S for Loam	25
19.	RCS vs. ϕ_S for Loam	26
20.	RCS vs. ϕ_S for Loam	27
21.	RCS vs. ϕ_S for Loam	28
22.	RCS vs. ϕ_S for Loam	29
23.	RCS vs. ϕ_S for Loam	30
24.	RCS vs. ϕ_S for Loam	31
25.	RCS vs. ϕ_S for Loam	32
26.	RCS vs. ϕ_S for Loam	33
27.	RCS vs. ϕ_S for Loam	34
28.	RCS vs. ϕ_S for Loam	35
29.	RCS vs. ϕ_S for Loam	36
30.	Bistatic Clutter Map for Loam (HH Polarization)	38
31.	Monostatic Clutter Map for Loam (HH Polarization)	39
32.	Monostatic/Bistatic Ratio Map for Loam (HH Polarization)	40
33.	Bistatic Clutter Map for Loam (VV Polarization)	41
34.	Monostatic Clutter Map for Loam (VV Polarization)	43
35.	Monostatic/Bistatic Ratio Map for Loam (VV Polarization)	44

The Validation and Application of a Bistatic Two-Scale of Surface Roughness Scattering Model

1. INTRODUCTION

Several new radar systems are being considered which operate in a bistatic mode. This offers the potential for increased target radar cross sections but has a more complicated clutter condition than typical monostatic operation would involve. This report addresses three topics related to this question. First, a bistatic terrain scattering model that includes two distinct sets of scattering phenomena¹ is evaluated by comparisons with some bistatic scattering data.² Secondly, the contributions from each of the levels of scattering are analyzed as a function of bistatic configuration. Finally, the validated bistatic scattering results are compared to a corresponding set of monostatic values representing a clutter map of a region where the surface is loam.

2. MODEL VALIDATION

In this section the two-scale-of-roughness bistatic scattering model will be described. Then the data base used for the comparisons will be discussed. Finally, the results for data and theory will be

(Received for Publication 25 October 1988)

1. Ruck, G.T., Barrick, D.E., Stuart, W.D., and Krichbaum, C.K. (1970) *Radar Cross Section Handbook*, Vol. 2, Plenum Press, New York.
2. Cost, S.T. (1965) *Measurements of the Bistatic Echo Area of Terrain at X-band*, Master's Thesis, Ohio State University.

examined as a function of the bistatic scattering angles. Figure 1 shows the angles involved. θ_g is the complement of θ_i , the incident elevation angle; θ_s is the scattered elevation angle; and ϕ_s is the azimuthal scattering angle. In the monostatic case $\phi_s = 180^\circ$.

2.1 Theory

The model is quite complex. Details are given here to make the comparisons with data clearer in terms of the use of parameter values associated with the particular scattering processes. Two distinct roughness elements are assumed to contribute to the scattering cross section σ° used in the scattering model. The large surface roughness is described by a model based upon physical optics (PO) assumptions. It can be shown that one sufficient condition for the validity of physical optics is that $T_L \gg \lambda$, where T_L is the surface correlation length associated with the large scale roughness. The form for σ° is in terms of the Rayleigh parameter $\Sigma = \frac{2\pi}{\lambda} \sigma_L (\cos \theta_i + \cos \theta_s)$. Here, σ_L = standard deviation in surface height for large scale roughness. When the conditions for the validity of physical optics are met, and the Rayleigh parameter $\Sigma \gg 1$, the form of σ° is equivalent to a high frequency, geometrical optics (GO) limit solution. The small scale surface roughness is described by the perturbation method (PM) solution.¹ The conditions for the validity of the perturbation solution are that the rms surface height be small compared to a wavelength ($2\pi/\lambda$) $\sigma_s < 1$ and that the surface slopes be small $\sigma_s/T_s < 1$, where σ_s = standard deviation in surface height for the small scale roughness and T_s = surface correlation length for small scale roughness. In general, the surface can be quite complex; its scattering contribution may have to be integrated over segments with different geological features. Here, we are concerned only with the behavior of σ° . The surface areas are assumed to have Gaussian height statistics. The surface correlation function is assumed to be Gaussian. Surface shadowing effects are also included in the formalism.

For physical optics models, Ruck et al¹ give expressions for the average bistatic rough surface cross section σ° under the following assumptions: (1) the radius of curvature of the surface irregularities is larger than a wavelength; (2) the roughness is isotropic in both surface dimensions; (3) the correlation length is smaller than either the x or y dimension of the sample subregion; and (4) multiple scattering is neglected. Using their notation, one finds that the expression for σ° becomes

$$\sigma^\circ = |\beta_{pq}|^2 J S \quad (1)$$

where β_{pq} represents the scattering matrix contributions, S is the local shadowing function, and the term J is related to the surface height distributions and the surface slopes. The shadowing function clearly depends on the roughness of the surface, and introducing this factor into the analysis can have significant effects on the diffuse scattered power.

In this report, the physical optics part of the theoretical cross section σ° is not evaluated in the high frequency geometrical optics limit. Instead, it is evaluated by making the assumption of small surface slopes $\sigma_L/T_L < 1$ so that J is expressed as a single integral (Papa et al³).

3. Papa, R.J., Lennon, J.F., and Taylor, R.L. (1984) *An Analysis of Physical Optics Models for Rough Surface Scattering*, RADC-TR-84-195, ADA 154960.

SURVEILLANCE GEOMETRIES

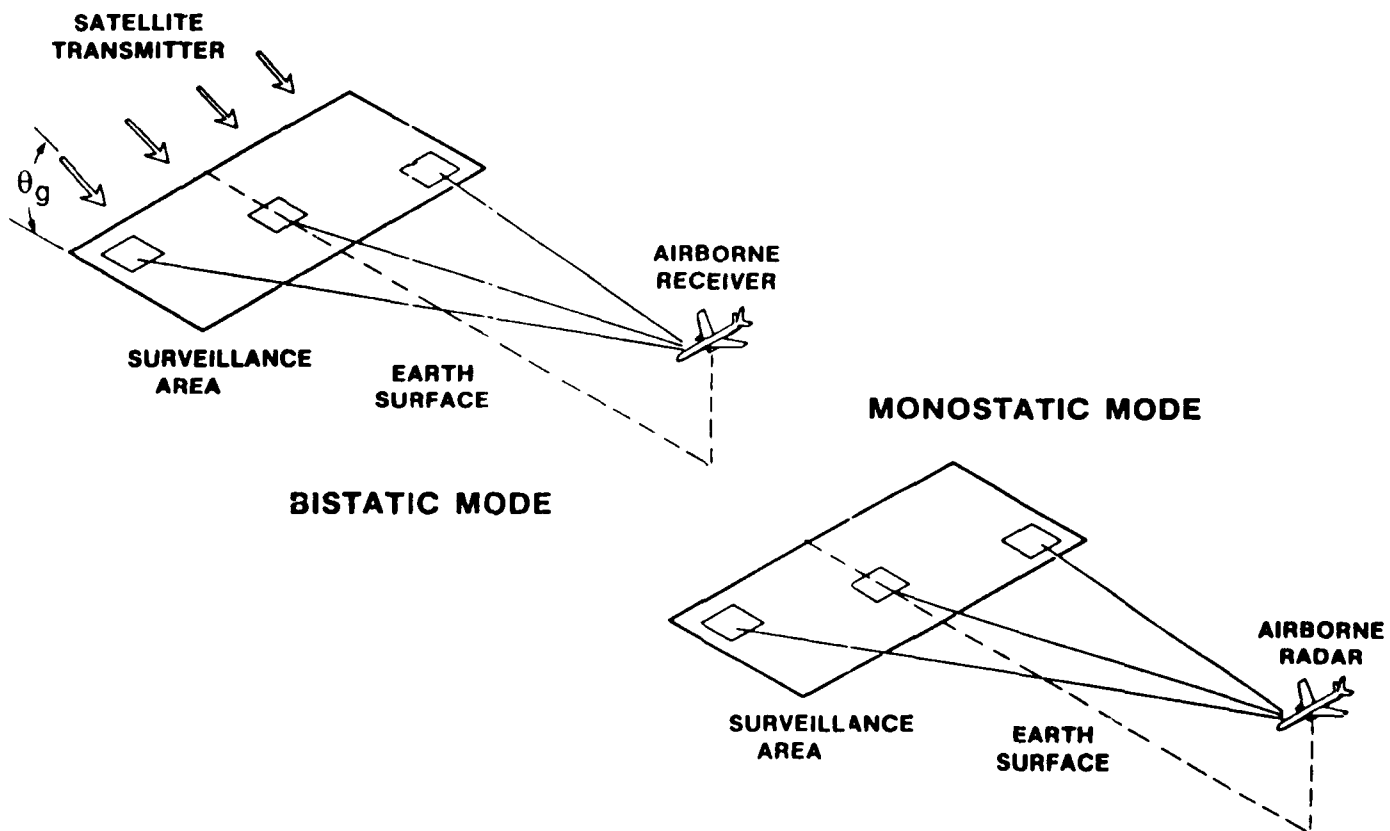


Figure 1. Surveillance Geometries for a Bistatic System or a Monostatic System

$$J = \frac{8\pi^2}{\lambda^2} \int_0^{\infty} J_0(v_{xy} \tau) [\chi_2 - \chi_1 \chi_1^*] \tau d\tau \quad (2)$$

where

$$v_{xy} = \sqrt{v_x^2 + v_y^2}$$

$$v_x = (2\pi/\lambda) \xi_x$$

$$v_y = (2\pi/\lambda) \xi_y$$

$\chi_1 = \varepsilon^{-\frac{1}{2}} \Sigma^2$, univariate characteristic function of the surface height distribution function

$\chi_2 = \exp[-\Sigma^2(1 - e^{-\tau^2/\Gamma^2})]$, bivariate characteristic function (Gaussian in this report)

J_0 is the zero order Bessel function.

here,

$$\xi_x = \sin \theta_i - \sin \theta_s \cos \phi_s .$$

$$\xi_y = \sin \phi_s \sin \theta_s .$$

$$\xi_z = -\cos \theta_i - \cos \theta_s .$$

It is in the scattering matrix term that the dielectric constant representing the respective moisture content levels is introduced. In that term, the matrix elements for linear polarization states are

$$\beta_{VV} = [a_2 a_3 R_{\parallel}(\theta_i^{\prime\prime}) + \sin \theta_i \sin \theta_s \sin^2 \phi_s R_{\perp}(\theta_i^{\prime\prime})] / [a_1 a_4] .$$

$$\beta_{HV} = \sin \phi_s [-\sin \theta_i a_3 R_{\parallel}(\theta_i^{\prime\prime}) + \sin \theta_s a_2 R_{\perp}(\theta_i^{\prime\prime})] / [a_1 a_4] . \quad (3)$$

$$\beta_{VH} = \sin \phi_s [\sin \theta_s a_2 R_{\parallel}(\theta_i^{\prime\prime}) - \sin \theta_i a_3 R_{\perp}(\theta_i^{\prime\prime})] / [a_1 a_4] .$$

$$\beta_{HH} = [-\sin \theta_i \sin \theta_s \sin^2 \phi_s R_{\parallel}(\theta_i^{\prime\prime}) - a_2 a_3 R_{\perp}(\theta_i^{\prime\prime})] / [a_1 a_4] .$$

Here, $R_{\parallel}(\theta_i^{\prime\prime})$ and $R_{\perp}(\theta_i^{\prime\prime})$ are Fresnel reflection coefficients

$$R_{\parallel}(\theta_i^{\prime\prime}) = [\varepsilon_r \cos \theta_i^{\prime\prime} - \sqrt{\varepsilon_r \mu_r - \sin^2 \theta_i^{\prime\prime}}] / [\varepsilon_r \cos \theta_i^{\prime\prime} + \sqrt{\varepsilon_r \mu_r - \sin^2 \theta_i^{\prime\prime}}] \quad (4)$$

and

$$R_{\perp}(\theta_i^{\prime\prime}) = [\mu_r \cos \theta_i^{\prime\prime} - \sqrt{\varepsilon_r \mu_r - \sin^2 \theta_i^{\prime\prime}}] / [\mu_r \cos \theta_i^{\prime\prime} + \sqrt{\varepsilon_r \mu_r - \sin^2 \theta_i^{\prime\prime}}] .$$

Note that ϵ_r is the relative complex dielectric constant of the surface, the subscript \parallel refers to the E-field in the plane of incidence, and the subscript \perp refers to the E-field normal to the plane of incidence. The remaining angle-related terms are

$$\cos \theta_1'' = (1/\sqrt{2}) \sqrt{1 - \sin \theta_1 \sin \theta_s \cos \phi_s + \cos \theta_1 \cos \theta_s}$$

$$a_1 = 1 + \sin \theta_1 \sin \theta_s \cos \phi_s - \cos \theta_1 \cos \theta_s .$$

$$a_2 = \cos \theta_1 \sin \theta_s + \sin \theta_1 \cos \theta_s \cos \phi_s .$$

$$a_3 = \sin \theta_1 \cos \theta_s + \cos \theta_1 \sin \theta_s \cos \phi_s .$$

and

$$a_4 = \cos \theta_1 + \cos \theta_s .$$

For small scale roughness the cross section, σ_{ss}^o is obtained by a perturbation method solution to Maxwell's equations. The fundamental assumptions for this case are small roughness ($k\sigma_s < 1$) and small surface slopes ($|\partial z_s/\partial x|, |\partial z_s/\partial y| < 1$) with isotropic roughness. Here, $k = 2\pi/\lambda$, and z_s is the surface height.

For this model we have

$$\sigma_{ss}^o = (4/\pi)k^4 \sigma_s^2 \cos^2 \theta_1 \cos^2 \theta_s |\alpha_{pq}|^2 I \quad (5)$$

where α_{pq} is proportional to the scattering matrix element and, for a Gaussian surface with Gaussian correlation

$$I = \pi T_s^2 \exp [-0.25k^2 T_s^2 (\xi_x^2 + \xi_y^2)] . \quad (6)$$

The α_{pq} terms are given by

$$\alpha_{III} = \frac{[(\mu_r - 1)(\mu_r \sin \theta_1 \sin \theta_s - \cos \phi_s \sqrt{\epsilon_r \mu_r - \sin^2 \theta_1} \sqrt{\epsilon_r \mu_r - \sin^2 \theta_s}) + \mu_r^2 (\epsilon_r - 1) \cos \phi_s]}{[\mu_r \cos \theta_1 + \sqrt{\epsilon_r \mu_r - \sin^2 \theta_1}] [\mu_r \cos \theta_s + \sqrt{\epsilon_r \mu_r - \sin^2 \theta_s}]} \quad (7)$$

$$\alpha_{VII} = \sin \phi_s \frac{\epsilon_r (\mu_r - 1) \sqrt{\epsilon_r \mu_r - \sin^2 \theta_1} - \mu_r (\epsilon_r - 1) \sqrt{\epsilon_r \mu_r - \sin^2 \theta_s}}{[\mu_r \cos \theta_1 + \sqrt{\epsilon_r \mu_r - \sin^2 \theta_1}] [\epsilon_r \cos \theta_s + \sqrt{\epsilon_r \mu_r - \sin^2 \theta_s}]}$$

$$\alpha_{IIV} = \sin \phi_s \frac{\epsilon_r (\mu_r - 1) \sqrt{\epsilon_r \mu_r - \sin^2 \theta_s} - \mu_r (\epsilon_r - 1) \sqrt{\epsilon_r \mu_r - \sin^2 \theta_1}}{[\epsilon_r \cos \theta_1 + \sqrt{\epsilon_r \mu_r - \sin^2 \theta_1}] [\mu_r \cos \theta_s + \sqrt{\epsilon_r \mu_r - \sin^2 \theta_s}]}$$

and

$$\alpha_{VV} = \frac{[(\epsilon_r - 1)(\epsilon_r \sin \theta_1 \sin \theta_s - \cos \phi_s \sqrt{\epsilon_r \mu_r - \sin^2 \theta_1} \sqrt{\epsilon_r \mu_r - \sin^2 \theta_s}) + \epsilon_r^2 (\mu_r - 1) \cos \phi_s]}{[\epsilon_r \cos \theta_1 + \sqrt{\epsilon_r \mu_r - \sin^2 \theta_1}] [\epsilon_r \cos \theta_s + \sqrt{\epsilon_r \mu_r - \sin^2 \theta_s}]}$$

In the previous equations, ϵ_r is the relative permittivity of the surface and μ_r is the relative permeability. They may be either real or complex (for a lossy surface). Here we take $\mu_r = 1$.

We have derived individual expressions for the cross section of the surface of each of the two levels of roughness to be considered. It has been shown that, as long as $\sigma_L/T_L < 1$ for the large scale roughness, the total scattering cross section is just the sum of the two components. If that is not the case, Brown⁴ has shown that the calculation of the composite cross section is no longer that simple. For our purposes we will address only cases that do satisfy the criterion, $\sigma_L/T_L < 1$, so that summation can be applied.

In this report, the surface heights are assumed to have a Gaussian distribution. Hence, the shadowing can be described (in the high frequency limit $\lambda \rightarrow 0$) by a shadowing function S derived by Sancer.⁵

(1) For $\phi_s = 180^\circ$,

$$S = 1/(1 + C_0) \text{ when } \theta_s < \theta_1 ;$$

$$S = 1/(1 + C_2) \text{ when } \theta_s \geq \theta_1 ; \text{ and}$$

(8)

(2) For $\phi_s \neq 180^\circ$,

$$S = 1/(1 + C_0 + C_2) .$$

In these expressions,

$$C_0 = [\sigma_L \tan \theta_1 / (T\sqrt{\pi})] \exp \left\{ -[T/(2\sigma_L \tan \theta_1)]^2 \right\} + (1/2) \operatorname{erfc} \left\{ T/(2\sigma_L \tan \theta_1) \right\}$$

and

$$C_2 = [\sigma_L \tan \theta_s / (T\sqrt{\pi})] \exp \left\{ -[T/(2\sigma_L \tan \theta_s)]^2 \right\} + (1/2) \operatorname{erfc} \left\{ T/(2\sigma_L \tan \theta_s) \right\}$$

Brown⁴ has shown that this shadowing function S multiplies the cross section for both large scale roughness and the cross section for the small scale roughness.

2.2 Data and Model Parameters

Cost² presents bistatic data in two formats. For $\phi_s = 0^\circ$, values of σ° are plotted as a function of elevation scattering angle θ_s , for fixed incident elevation angles θ_1 . In the second series of data sets the values of σ° are plotted as a function of azimuthal scattering angle for fixed values of $\theta_1 = \theta_s$. Both vertical-vertical and horizontal-horizontal polarized signals were considered and the data are for a

4. Brown, G.S. (1978) Backscattering from a Gaussian distributed, perfectly conducting, rough surface, *IEEE Trans. Antennas Propag.* **AP-26**:472-482.

5. Sancer, M.I. (1969) Shadow corrected electromagnetic scattering from a randomly rough surface, *IEEE Trans. Antennas Propag.* **AP-17**:577-585.

wavelength $\lambda = 3$ cm. (X-band). Only limited ground truth was given for the data. For the azimuthal variations we will show comparisons for loam. Cost gives the standard deviation in surface heights for his loam data to be on the order of a wavelength. The $\phi_s = 0^\circ$, elevation angle σ° comparisons in this report are for sand. Cost gives the standard deviation of the surface heights for sand as several wavelengths. For the loam comparisons, three sets of elevation angles were considered: $\theta_1 = \theta_s = 60^\circ$, $\theta_1 = \theta_s = 70^\circ$, and $\theta_1 = \theta_s = 85^\circ$. The $\phi_s = 0^\circ$ sand comparisons are made for two sets of incident angles, $\theta_1 = 20^\circ$ and $\theta_s = 40^\circ$.

The model parameters have to be related to the scattering surfaces that resulted in the experimental data sets. The parameters must have physically realistic values and are required to satisfy a series of constraints imposed by the model. First, the surface must be very large compared to the large scale correlation length. Next, the large scale surface slopes must be small, so that $T_L > \sigma_L$. The small scale surface parameters must satisfy the requirements that $T_s \ll T_L$ and $\sigma_s \ll \sigma_L$. Also, the small scale surface parameters must satisfy two additional constraints: (1) $\frac{2\pi}{\lambda} \sigma_s < 1$ and $\sigma_s/T_s < 1$. Subject to all these conditions, some variation in the surface is possible and there was no additional ground truth supplied by Cost. The principal model parameter of interest is the correlation length T_L . The constraints for this parameter for loam are such that $0.06 \text{ m} < T_L < 0.6 \text{ m}$ and for sand $0.15 \text{ m} < T_L < 0.6 \text{ m}$. The final selection of parameters was made by considering several possibilities and checking agreement with a limited data set. The same parameters were then used to predict behavior for other cases and the results are assessed in the next section. As an example, for the azimuthal cases, small incident elevation angle cases with horizontally polarized signals were used to establish the basic parameter set consistent with the parameter constraints of the model. For loam the final parameter values are $\sigma_L^2 = 0.03 \text{ m}$ (given); $T_L = 0.15 \text{ m}$ (mid-range); $\sigma_s^2 = 0.0045 \text{ m}$; $T_s = 0.025 \text{ m}$; and $\epsilon = 30.0 + j 2.0$. For sand, the corresponding baseline parameters are slightly different. Here, $\sigma_L^2 = 0.09 \text{ m}$ (given); $T_L = 0.45 \text{ m}$ (mid-range); $\sigma_s^2 = 0.0001 \text{ m}$; $T_s = 0.0005 \text{ m}$; and $\epsilon = 3.0 + j 0.2$.

2.3 Comparisons of Model Results with Data

The two-scale-of-roughness model predictions are compared to the X-band data taken by Cost. The loam data allows azimuthal variations to be examined while the sand results show scattering elevation variations for $\phi_s = 0^\circ$.

Figures 2 through 7 show Cost's data for loam as points for $\theta_1 = \theta_s = 60^\circ$, 70° , and 85° for both HH and VV polarizations. The solid lines show the theoretical model results with the two scales of roughness parameters chosen by judicious variations over a range of conditions. The dots show the experimental data. The final selection of parameters has been cited previously. The agreement between the experimental data and the theoretical model is, in general, good, considering the large variations in angles of incidence, scattering angles and polarizations. It should be noted that the general trend of σ° vs ϕ_s is followed by both the experimental data and the theoretical model. For small ϕ_s ($\phi_s = 0^\circ$), σ° is at a maximum; as ϕ_s increases, σ° reaches a minimum ($20^\circ < \phi_s < 100^\circ$); and then σ° increases and reaches a plateau beyond $\phi_s = 100^\circ$. This is true for $\theta_1 = \theta_s = 60^\circ$ and 70° , in terms of both the experimental data and the theoretical model, for both polarizations. The agreement between the experimental data and the theoretical model is the least good for $\theta_1 = \theta_s = 85^\circ$. This is probably due to the fact that here multiple scattering plays a role, and the two-scale model (with shadowing) doesn't

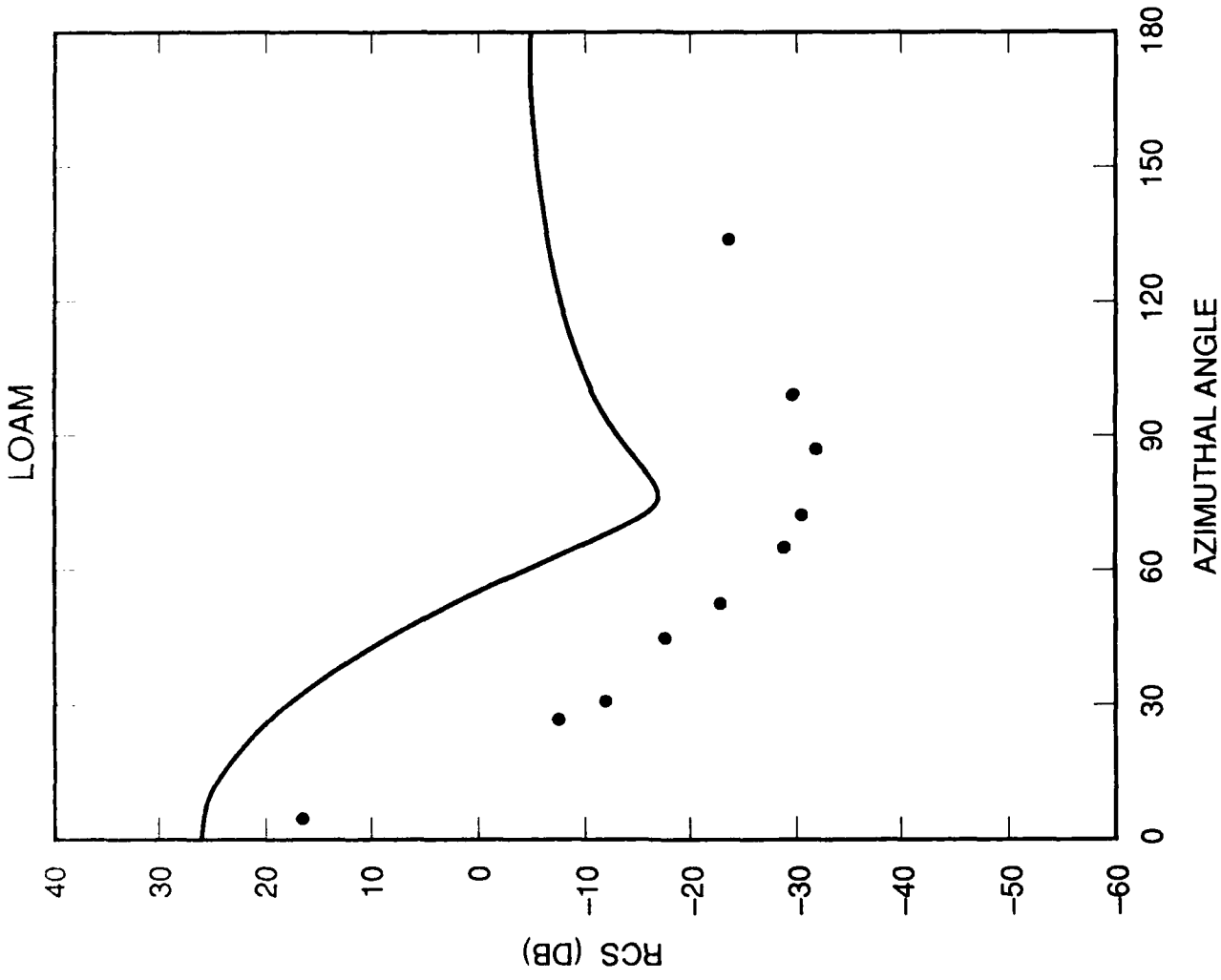
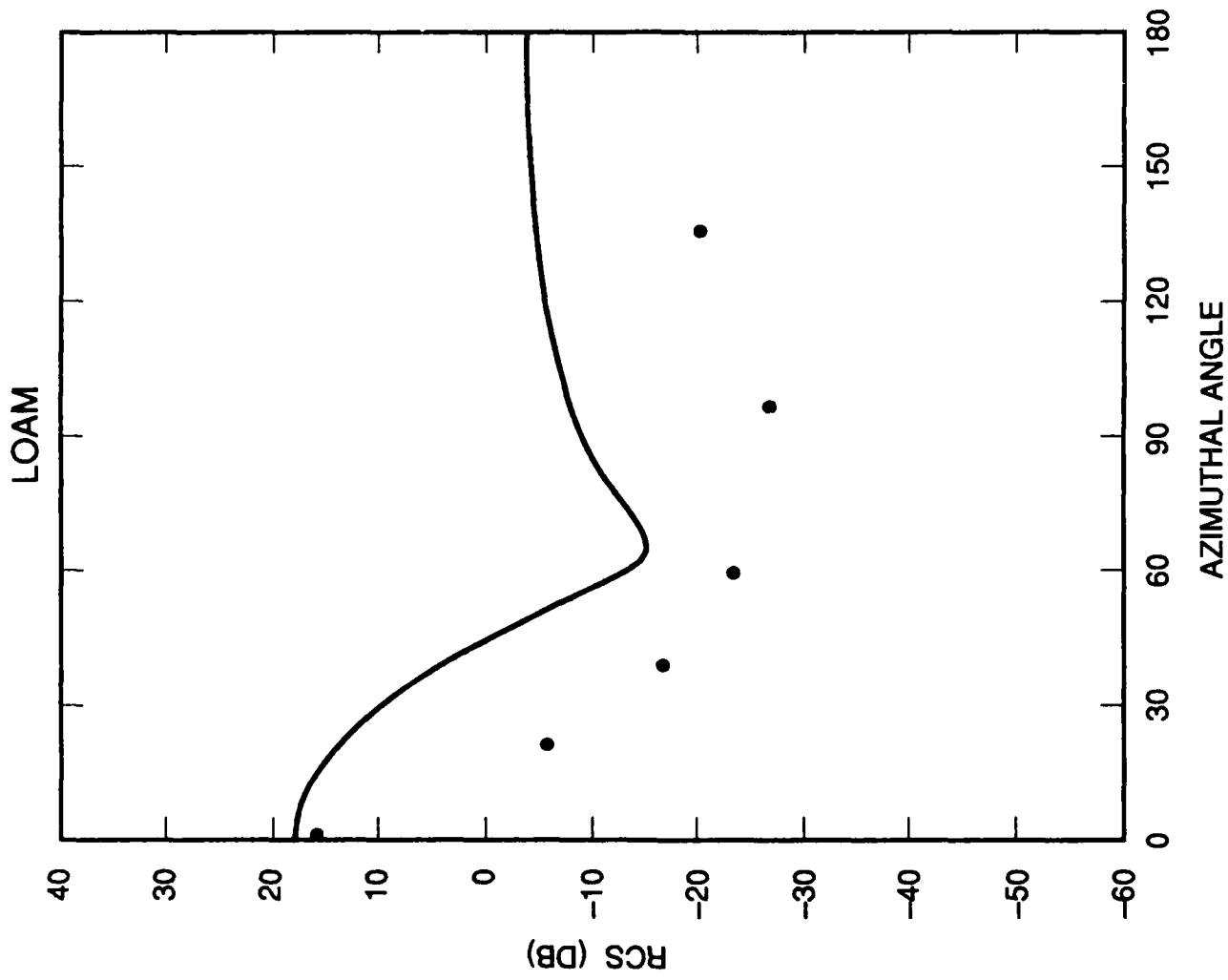
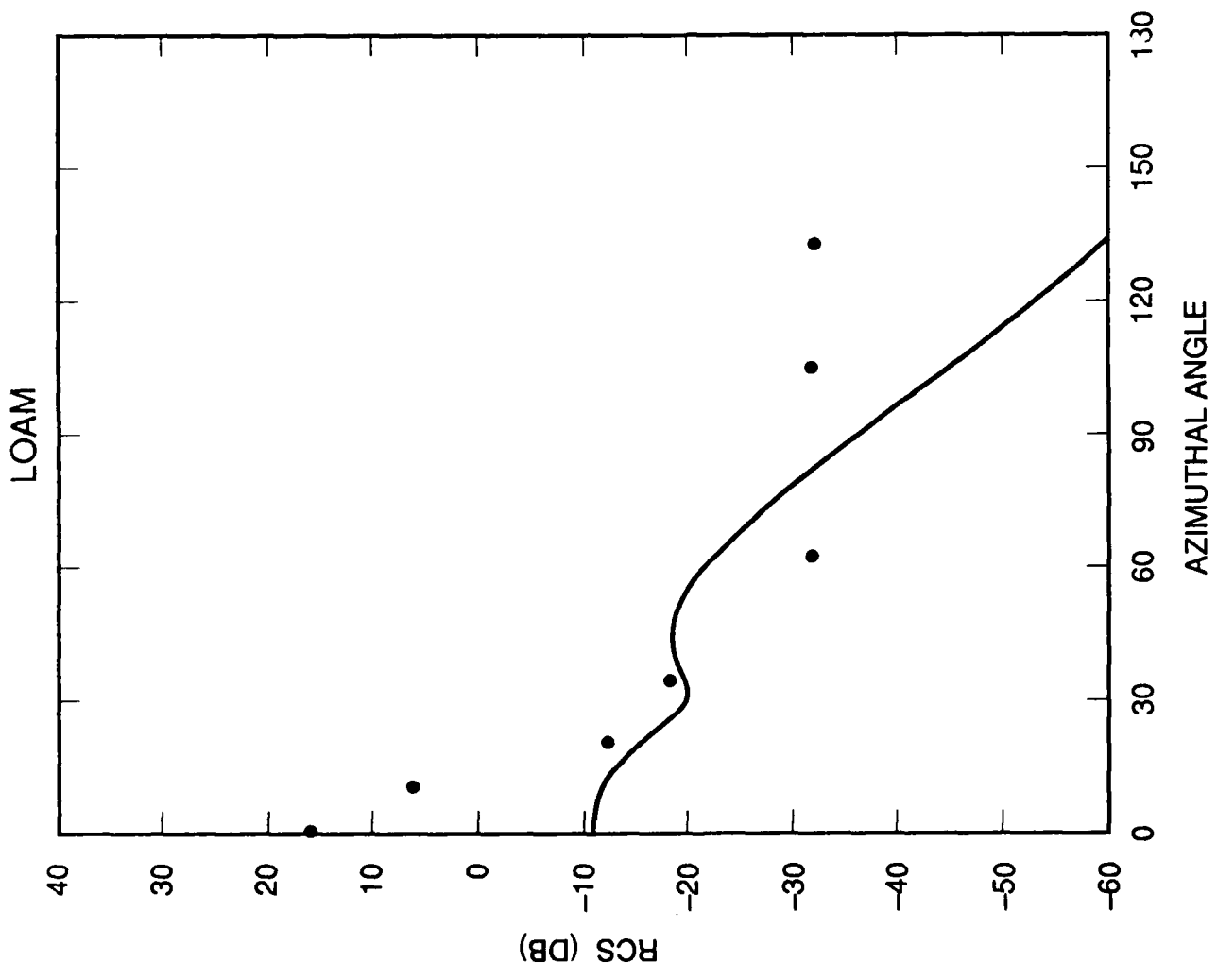


Figure 2. RCS vs. ϕ_s for Loam



θ_i 70.00
 θ_s 70.00
 λ 0.03
 σ_L^2 0.300E-01
 T_L 0.150
 σ_S^2 0.450E-02
 T_S 0.250E-01
 ϵ (30., 2.)
 HH Polarization
 Shadowing
 Gaussian Correlation
 Large Scale
 Small Scale

Figure 3. RCS vs. ϕ_s for Loam



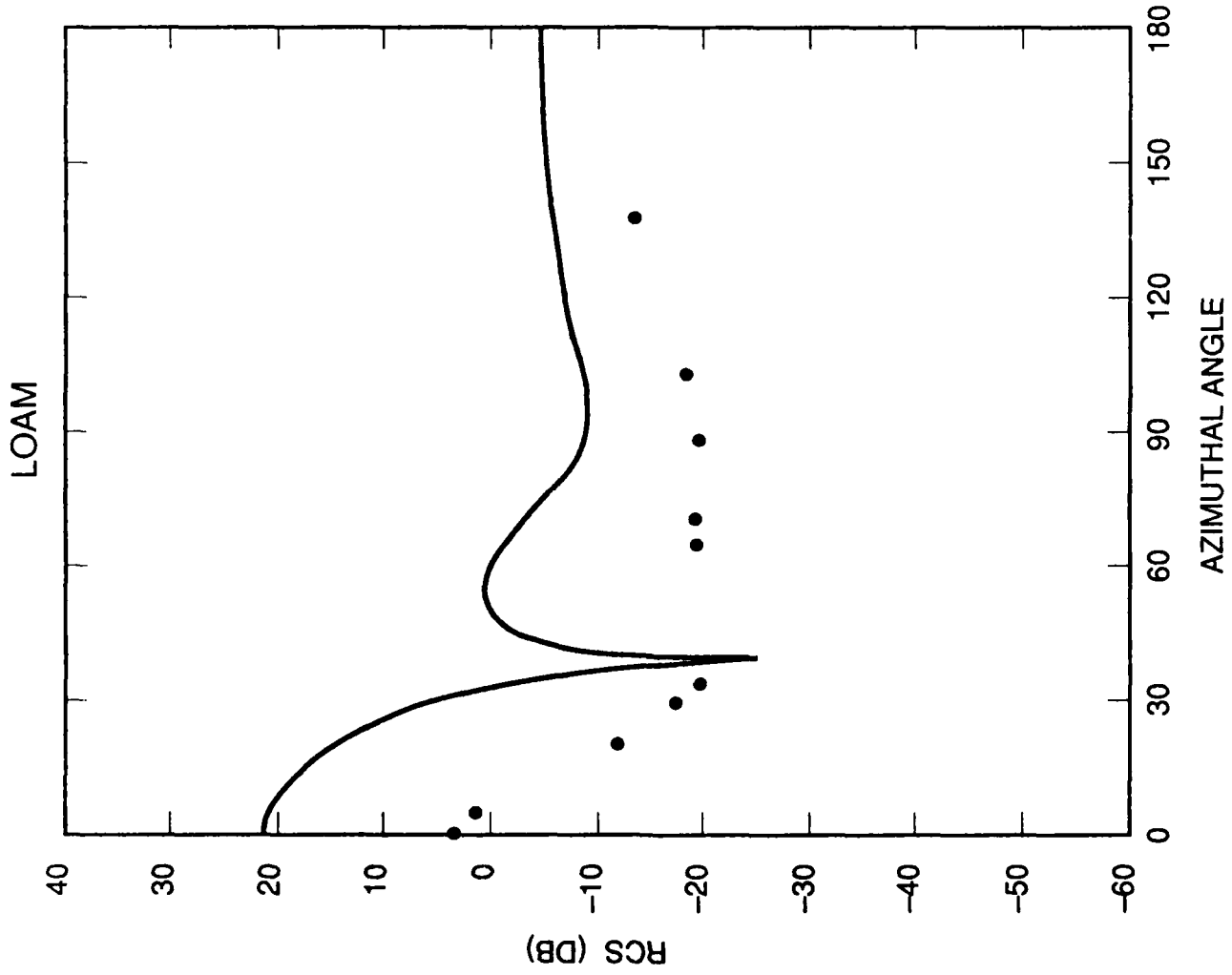
θ_i 85.00
 θ_s 85.00
 λ 0.03

σ_L^2 0.300E-01
 T_L 0.150
 σ_S^2 0.450E-02
 T_S 0.250E-01

ϵ (30., 2.)

HH Polarization
 Shadowing
 Gaussian Correlation
 Large Scale
 Small Scale

Figure 4. RCS vs. ϕ_s for Loam



θ_i 60.00
 θ_s 60.00
 λ 0.03

σ_L^2 0.300E-01
 T_L 0.150
 σ_S^2 0.450E-02
 T_S 0.250E-01

ϵ (30., 2.)

VV Polarization

Shadowing

Gaussian Correlation

Large Scale

Small Scale

Figure 5. RCS vs. ϕ_S for Loam

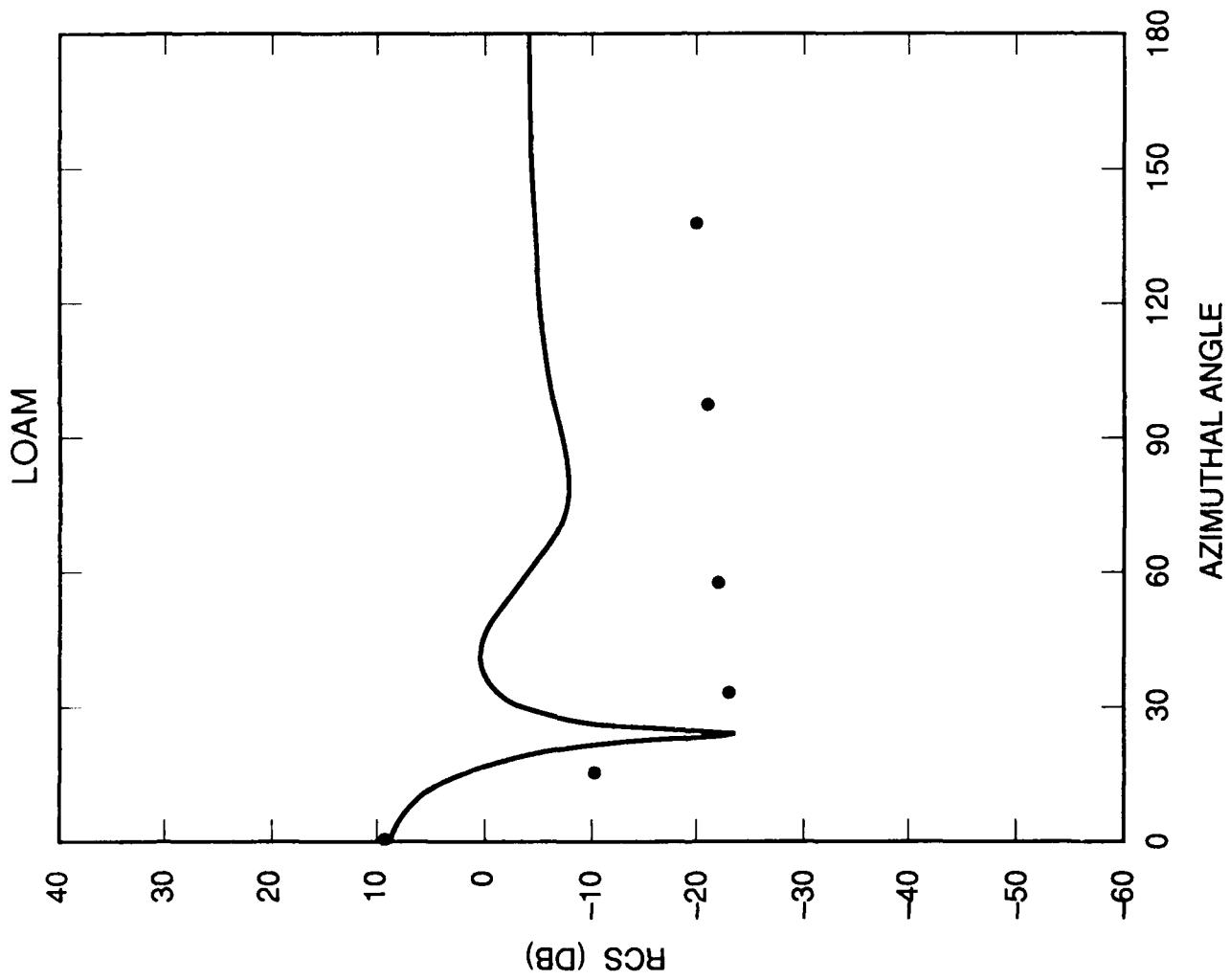


Figure 6. RCS vs. ϕ_s for Loam

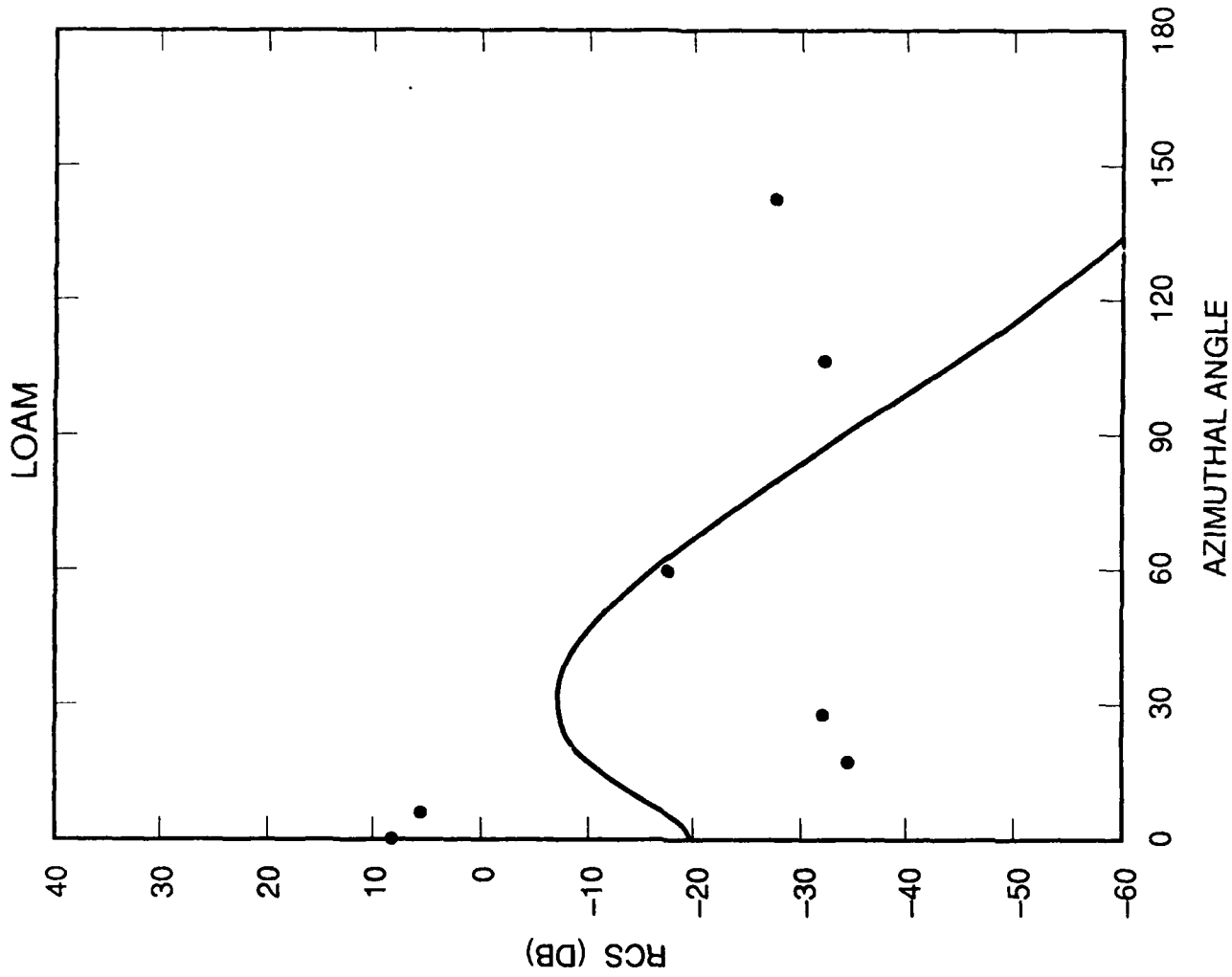


Figure 7. RCS vs. ϕ_s for Loam

account for multiple scattering. Also, the nulls in σ° shown in the theoretical curves near $\phi_s = 30^\circ$ in Figures 5 and 6 do not appear in the experimental data. This may occur because the nulls are narrow and there are simply not enough experimental data points in this region.

Figures 8 through 11 show Cost's data for sand as points for $\theta_1 = 20^\circ$ and 40° for both HH and VV polarizations. Again, the solid lines show the theoretical model results for the two scales of roughness parameters chosen in accord with Cost's data. The agreement between the experimental data and the theoretical model is quite good, and, in general, better than the agreement for loam. The greatest discrepancy between the experimental data and the theoretical model occurs for $\theta_s \rightarrow 90^\circ$. This discrepancy again may be attributed to the effects of multiple scattering, which mostly occur near small grazing angles. Also, there may be large errors in the experimental data when $\theta_s \rightarrow 90^\circ$, because it is difficult to define precisely the radar footprint on the earth's surface.

3. ASSESSMENT OF SURFACE ROUGHNESS CONTRIBUTIONS

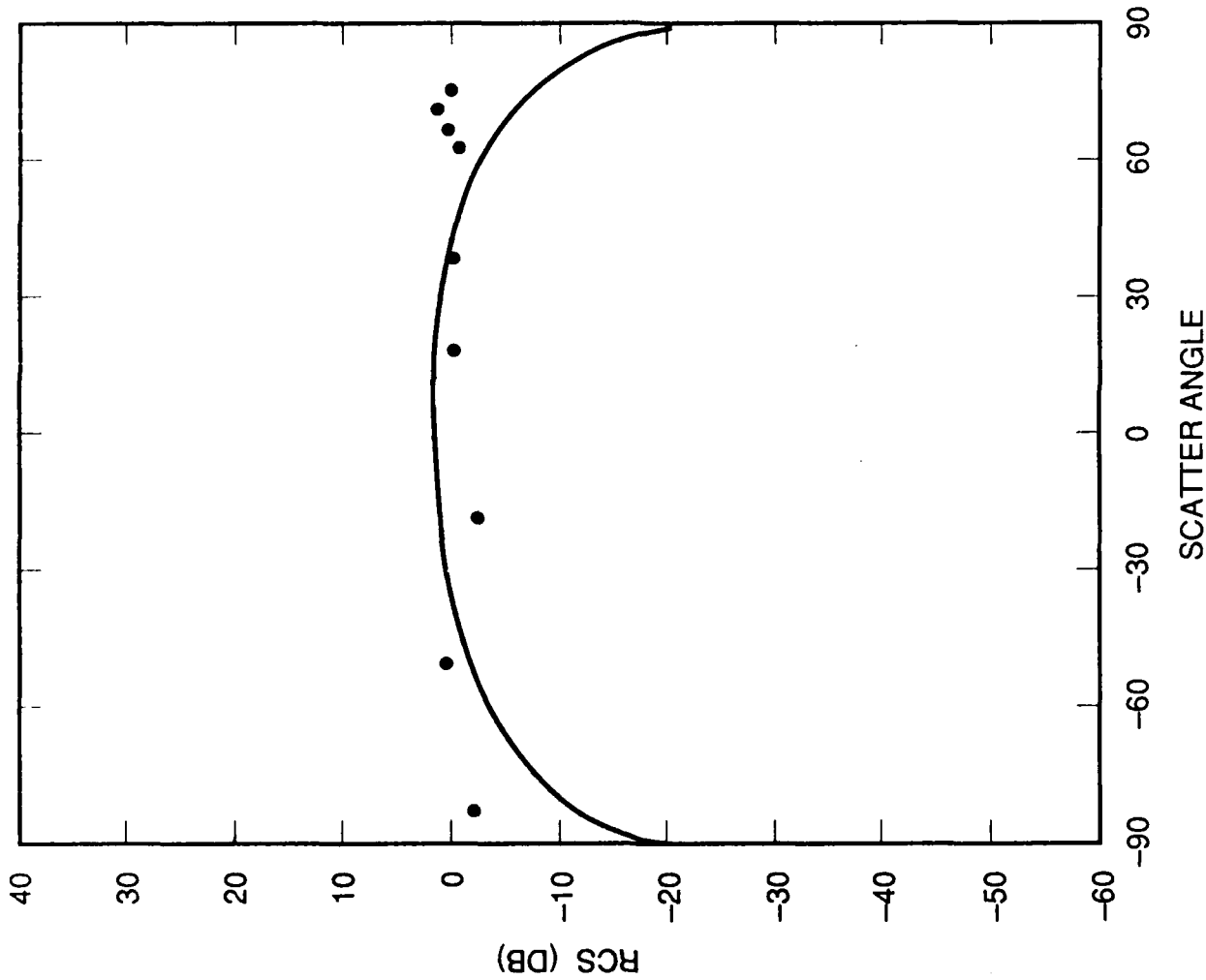
In the previous section we have shown how the two-scale model scattering predictions behave as a function of geometry. In this section we will examine the results more explicitly. The predictions will be examined with the contribution of each level of roughness isolated from the other so that the regions where one or the other scattering mechanism dominates the cross section can be seen and analyzed. Only horizontal-horizontal (HH) polarization results will be considered, since the behavior for the vertical-vertical (VV) polarization is very similar. Figures 12 through 20 show σ° vs ϕ_s plots for HH polarization for the large scale of roughness only (loam is the dielectric surface). Here, the surface slopes are small, $\sigma_L/T_L = 0.333$ for Figures 12, 13, and 14; and $\sigma_L/T_L = 0.577$ for Figures 15, 16, and 17.

The figures show, in general, a characteristic trend. The normalized cross section σ° starts out at a relatively high value at $\phi_s = 0^\circ$, drops down to some minimum value as ϕ_s increases, and then rises to a plateau as ϕ_s further increases. This behavior is not always exhibited when $\theta_1 = \theta_s = 85^\circ$, where σ° often exhibits a monotonic decrease as ϕ_s increases. The more general behavior which is shown at $\theta_1 = \theta_s = 60^\circ$ and 70° follows what is observed experimentally. Comparing Figure 15 with Figure 12, Figure 16 with Figure 13, and Figure 17 with Figure 14, one may observe another general trend in behavior. As the surface slope σ_L/T_L increases, σ° decreases near $\phi_s \equiv 0^\circ$ and σ° increases for $\phi_s >$ the null angle.

Figures 18, 19, and 20 summarize clearly the effects of σ_L and T_L on the graphs of σ° vs. ϕ_s for fixed θ_1 . Comparing Figure 19 with Figure 18, one may observe a general trend: as T_L increases, the right hand side (backscatter) decreases and the left hand side (forward scatter) increases (for σ_L constant, both HH and VV polarizations). Comparing Figure 20 with Figure 19, we may note that as σ_L decreases, the right hand side (backscatter) decreases and the left hand side (forward scatter) increases. Thus, for the large scale roughness, both T_L and σ_L control the shape of the σ° vs. ϕ_s curves.

In Figures 21 through 29, only the small scale roughness, (σ_s, T_s) contributes to the normalized cross section σ° . Comparing Figure 24 with Figure 21, Figure 25 with Figure 22, and Figure 26 with Figure 23, one may observe a trend in behavior that is analogous to the large-scale-of-roughness case. As T_s decreases (and σ_s/T_s , the slope, increases), σ° decreases near $\phi_s \equiv 0^\circ$ and σ° increases for $\phi_s > 30^\circ$.

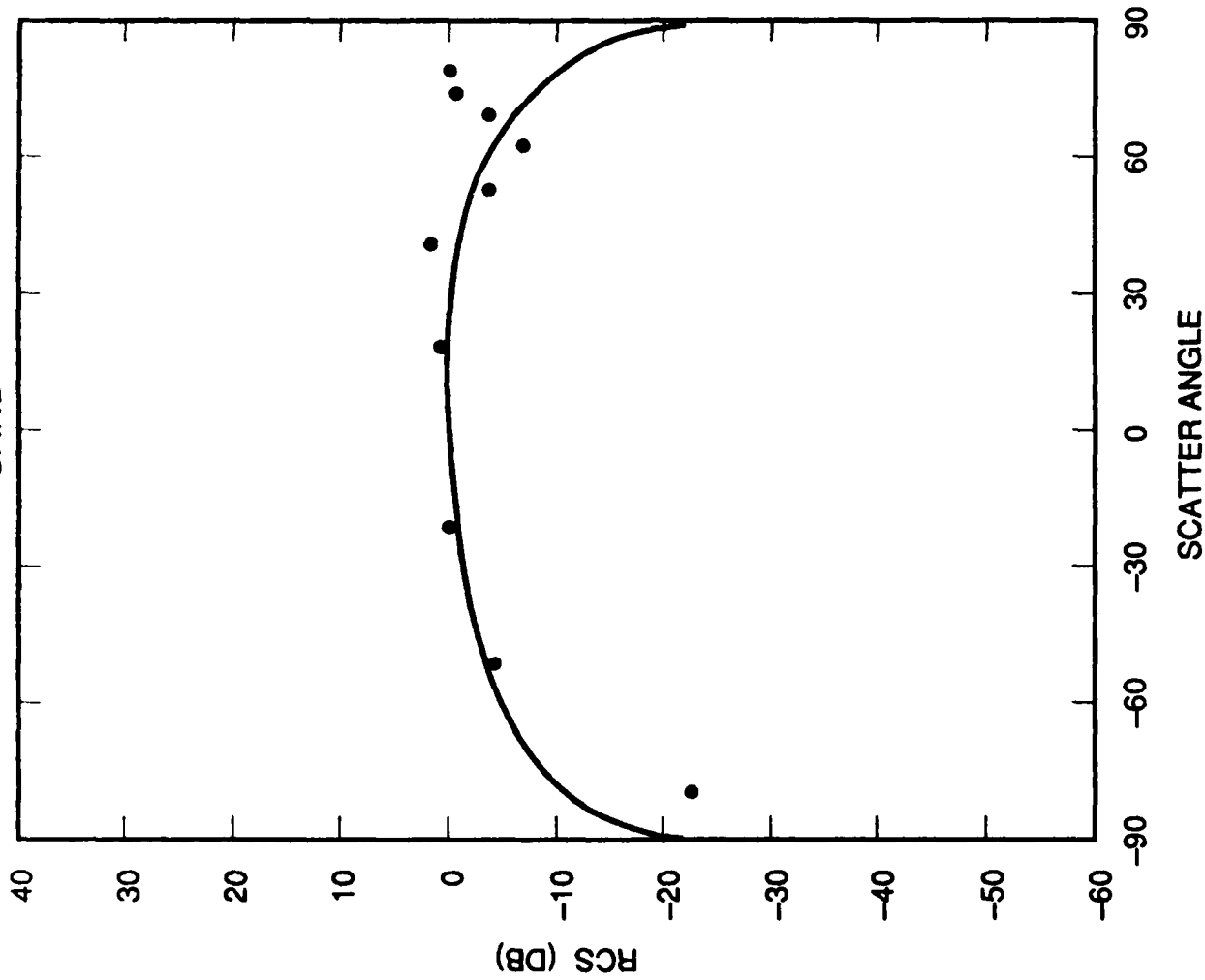
SAND



θ_i 20.00
 ϕ_s 0.00
 λ 0.03
 σ_L^2 0.900E-01
 T_L 0.450
 σ_S^2 0.100E-03
 T_S 0.500E-02
 ϵ (3.0, 0.2)
 HH Polarization
 Shadowing
 Gaussian Correlation
 Large Scale
 Small Scale

Figure 8. RCS vs. θ_s for Sand

SAND



θ_i 40.00

ϕ_s 0.00

λ 0.03

σ_L^2 0.900E-01

T_L 0.450

σ_s^2 0.100E-03

T_s 0.500E-02

ϵ (3.0, 0.2)

HH Polarization

Shadowing

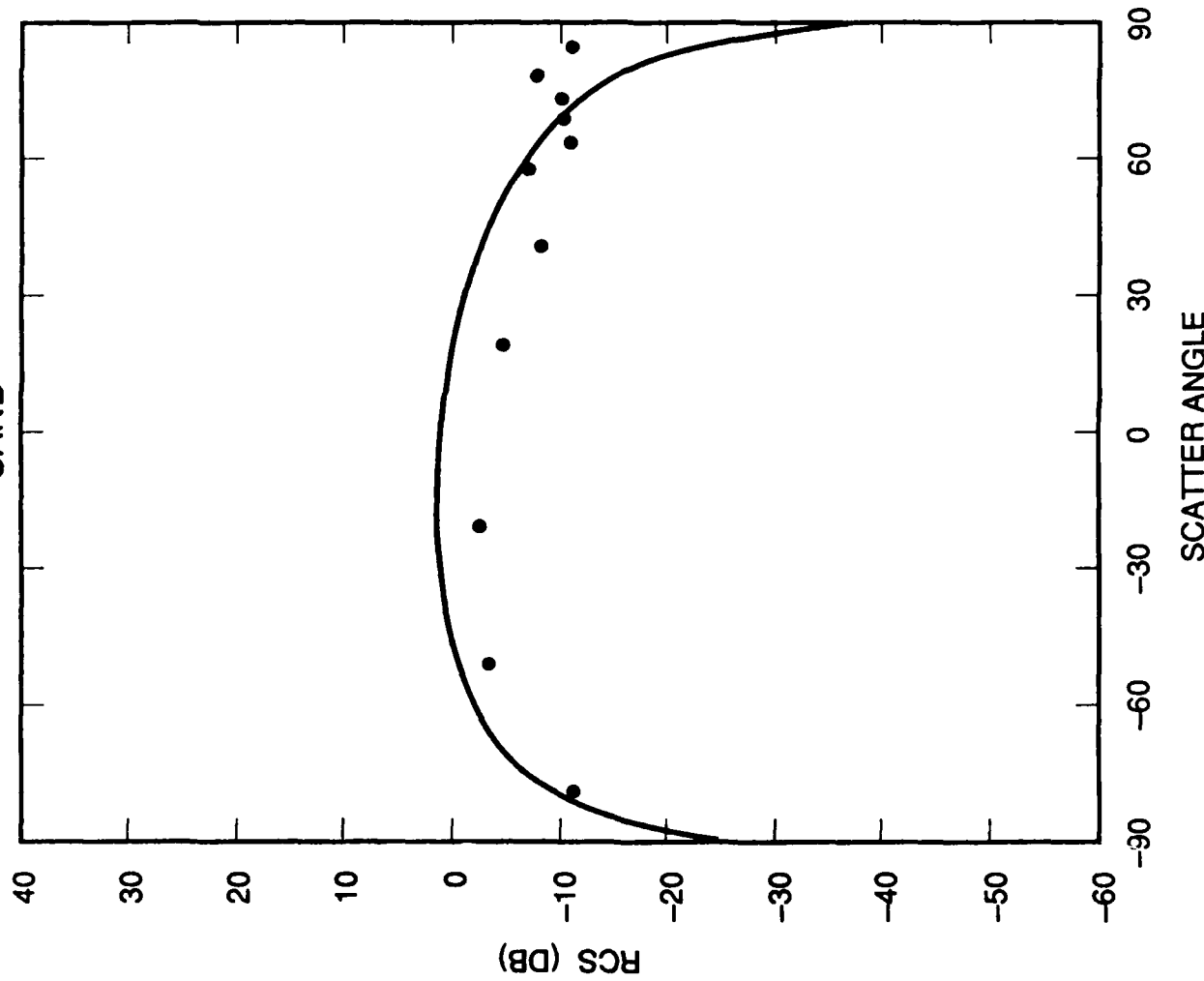
Gaussian Correlation

Large Scale

Small Scale

Figure 9. RCS vs. θ_s for Sand

SAND



θ_i	20.00
ϕ_s	0.00
λ	0.03
σ_L^2	0.900E-01
T_L	0.450
σ_S^2	0.100E-03
T_S	0.500E-02
ϵ	(3.0, 0.2)
VV Polarization	
Shadowing	
Gaussian Correlation	
Large Scale	
Small Scale	

Figure 10. RCS vs. θ_s for Sand

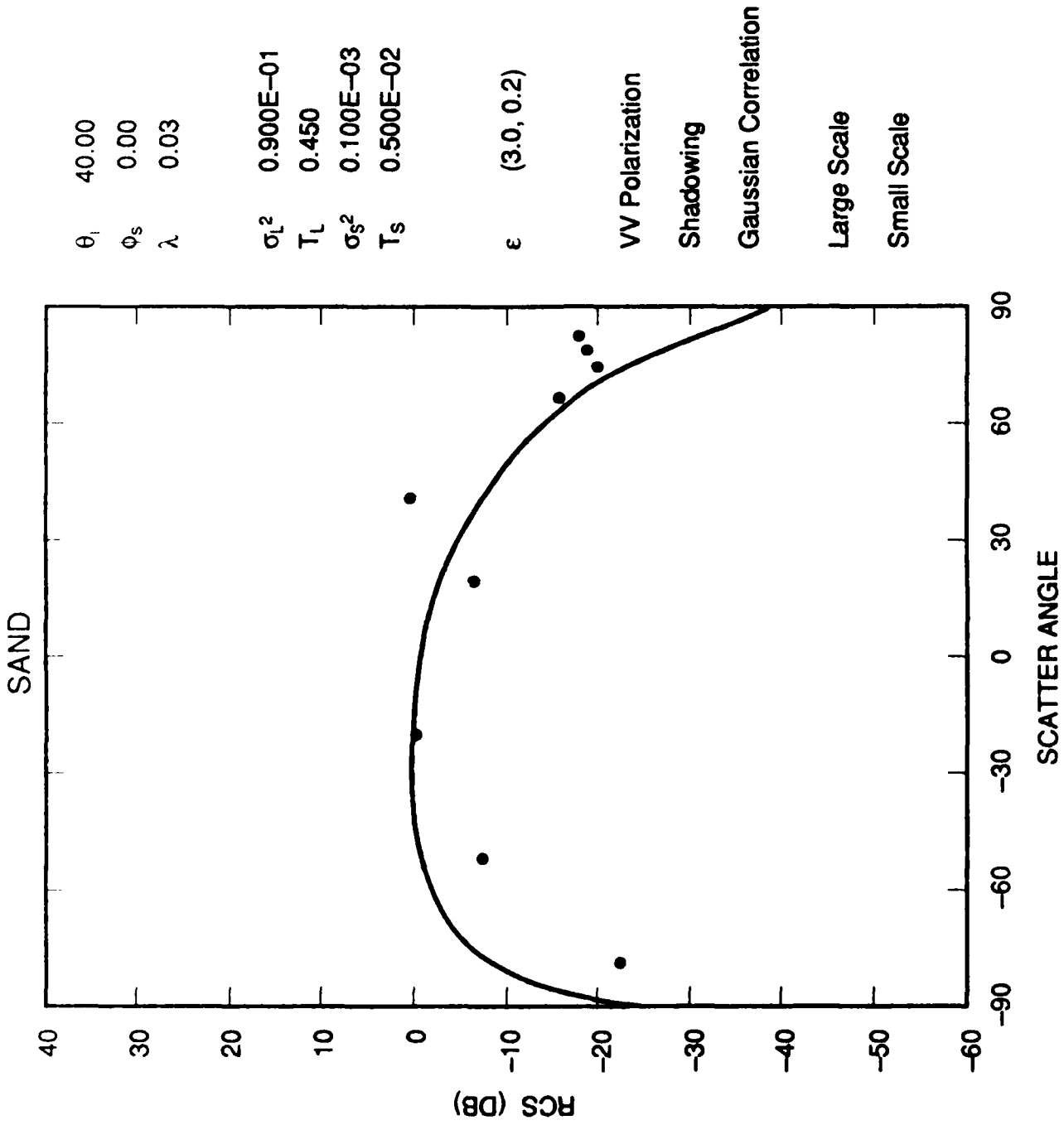


Figure 11. RCS vs. θ_s for Sand

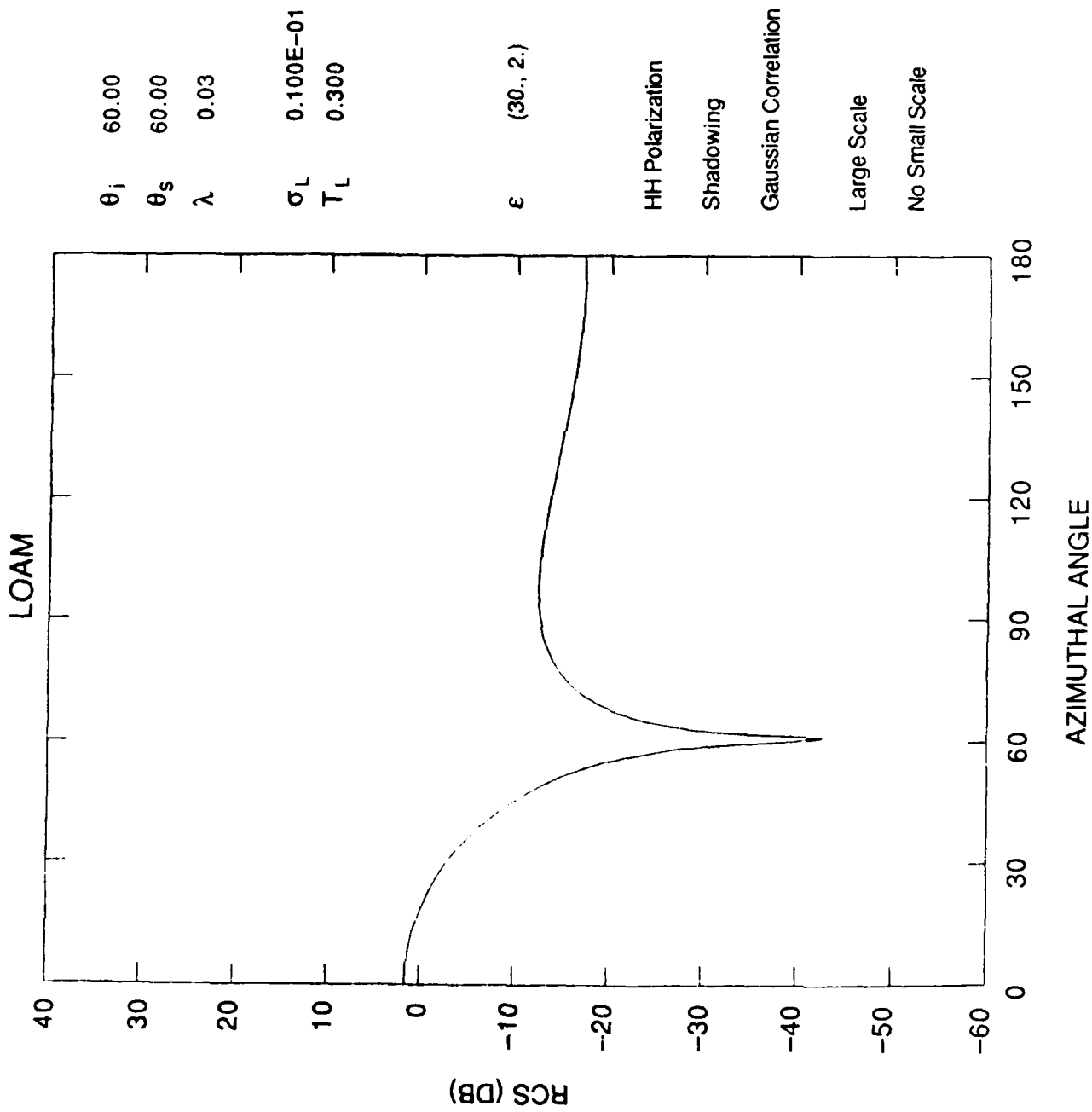


Figure 12. RCS vs. ϕ_s for Loam

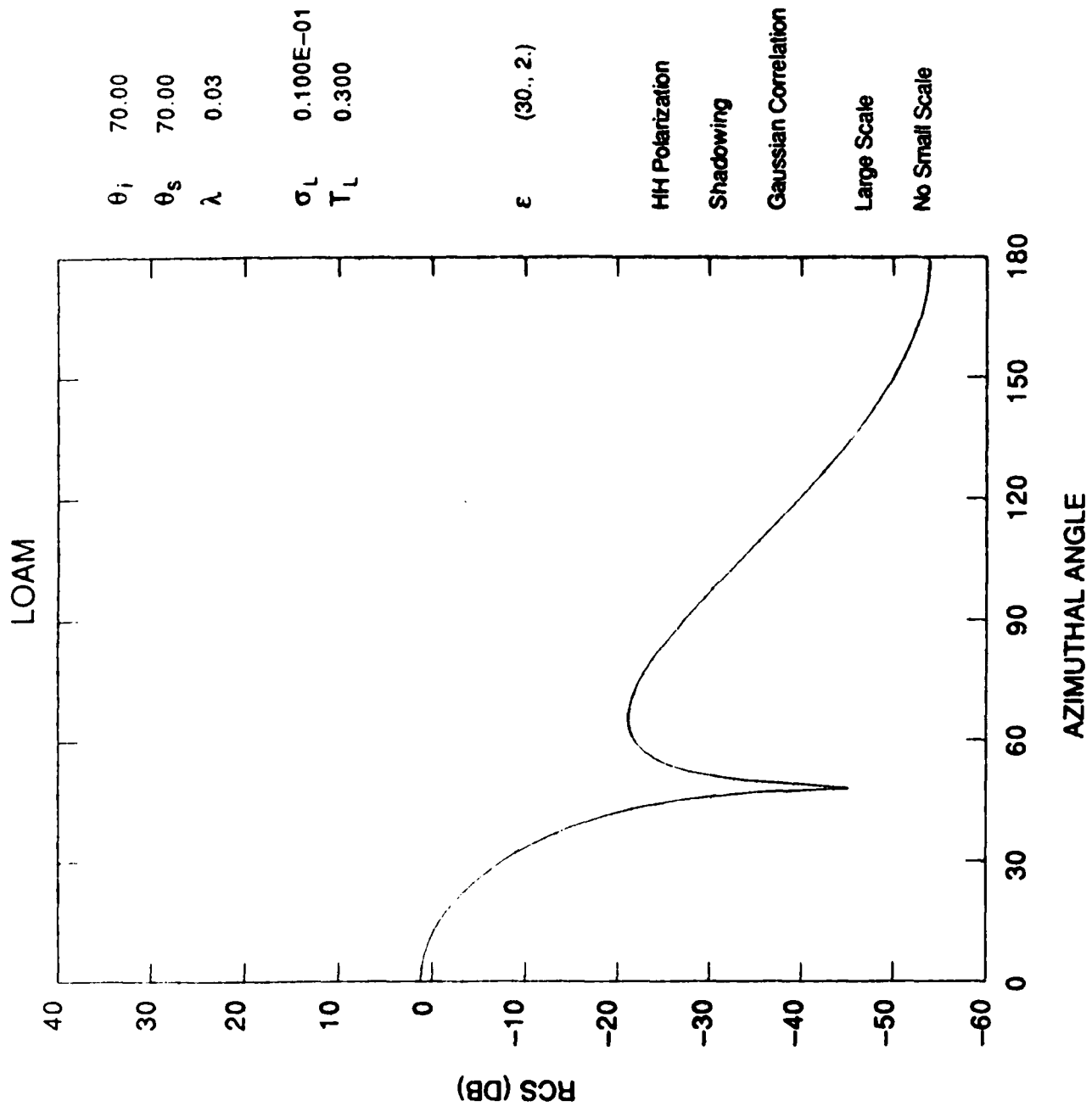


Figure 13. RCS vs. ϕ_s for Loam

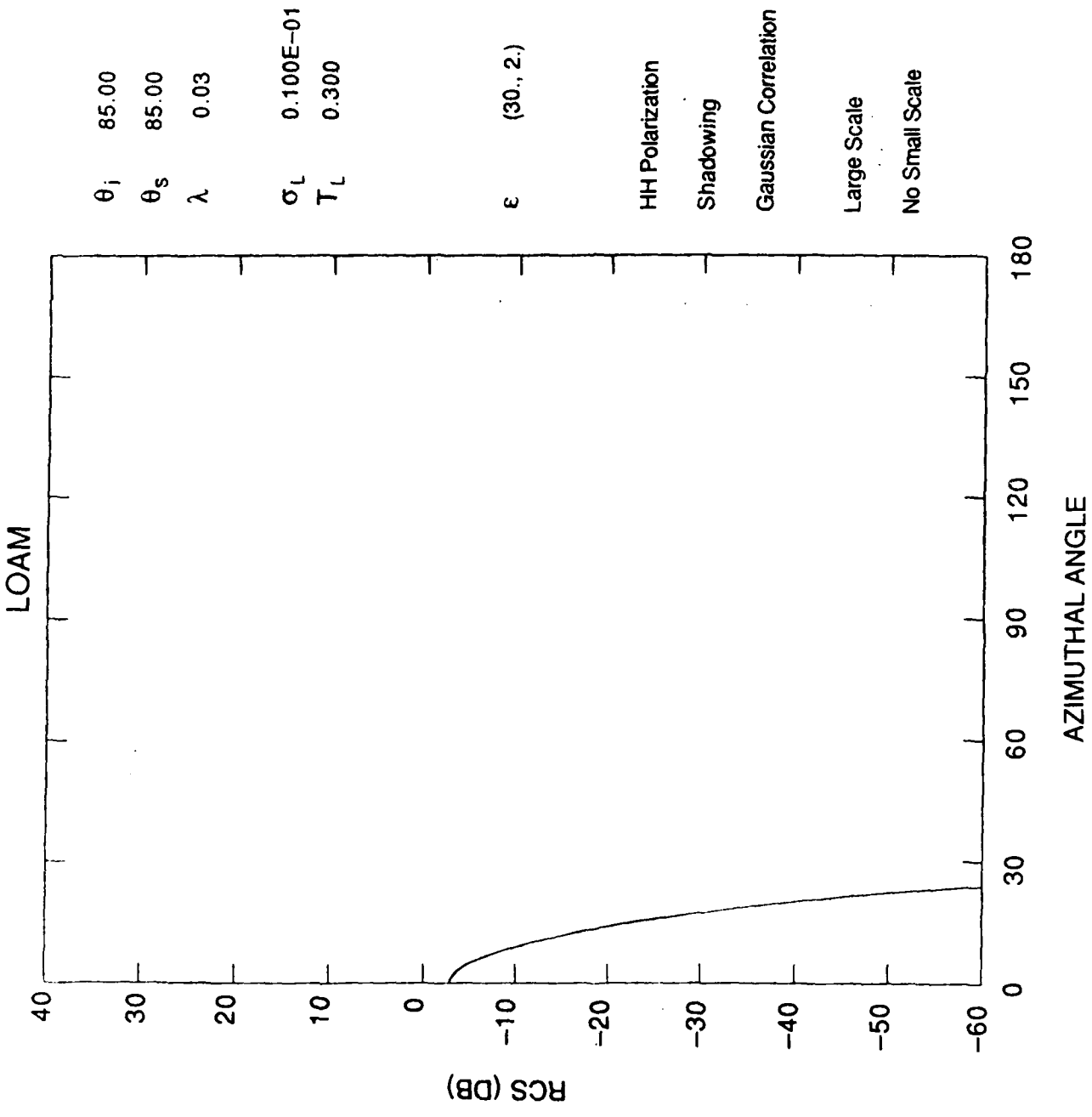


Figure 14. RCS vs. ϕ_s for Loam

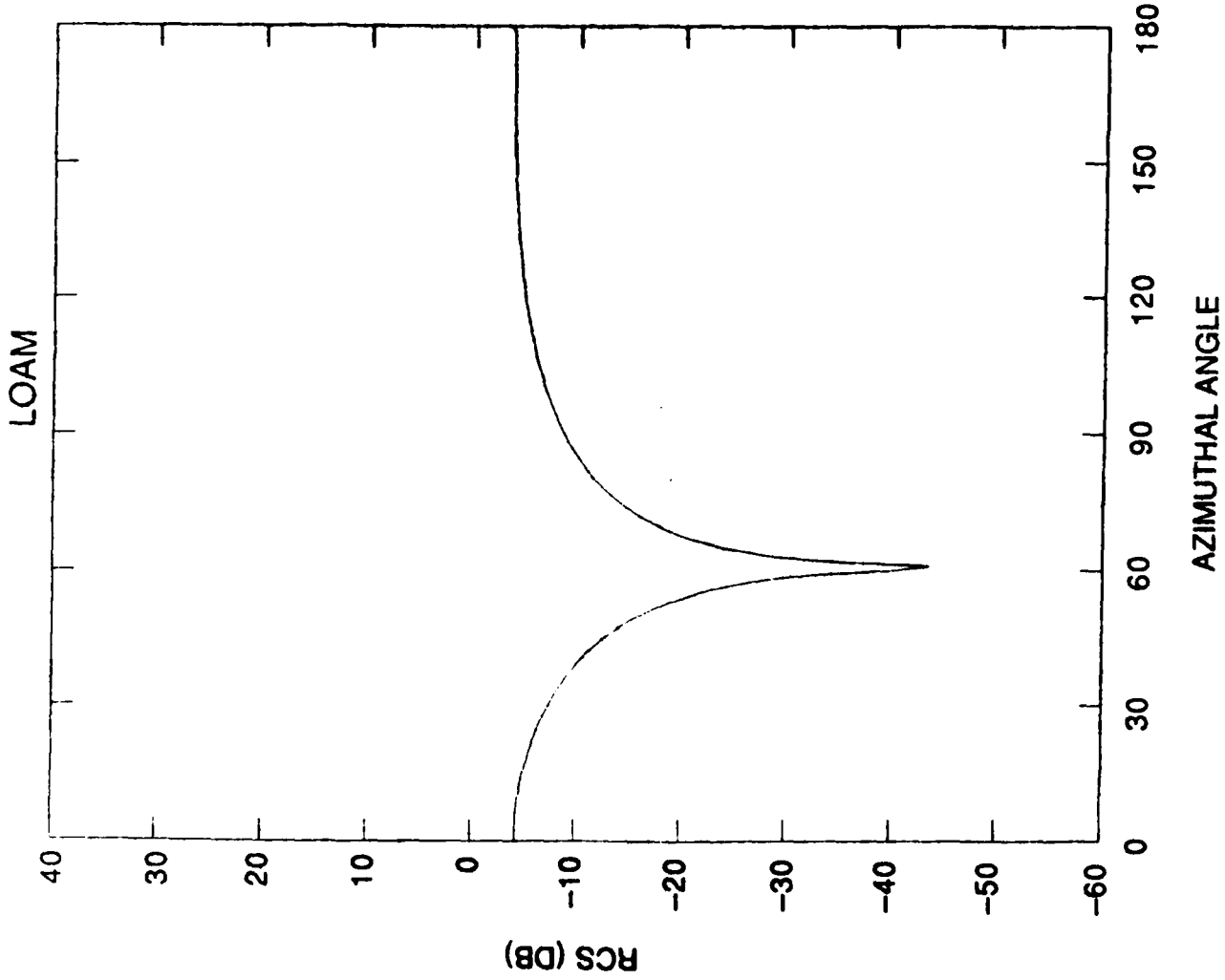


Figure 15. RCS vs. ϕ_s for Loam

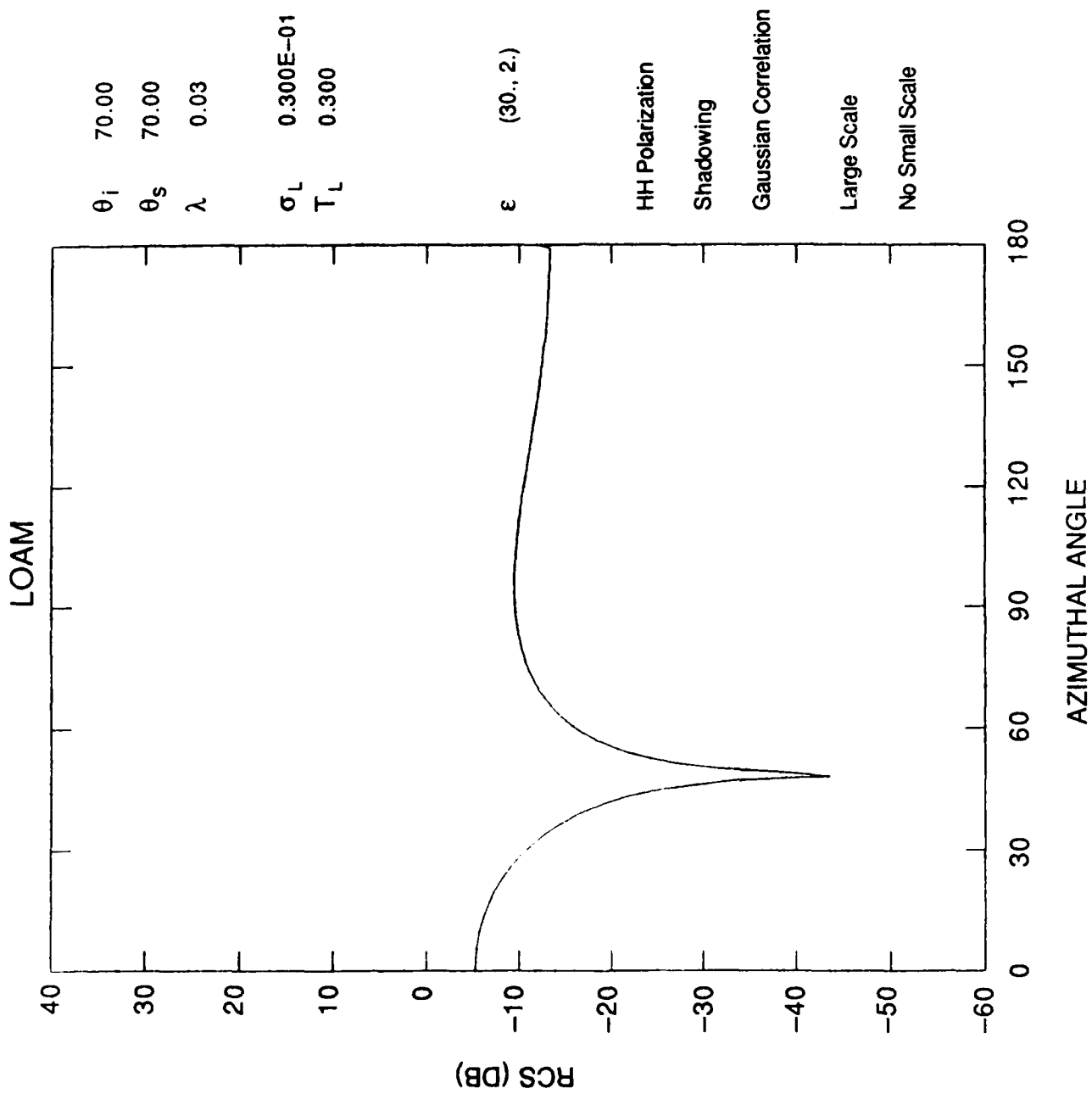


Figure 16. RCS vs. ϕ_s for Loam

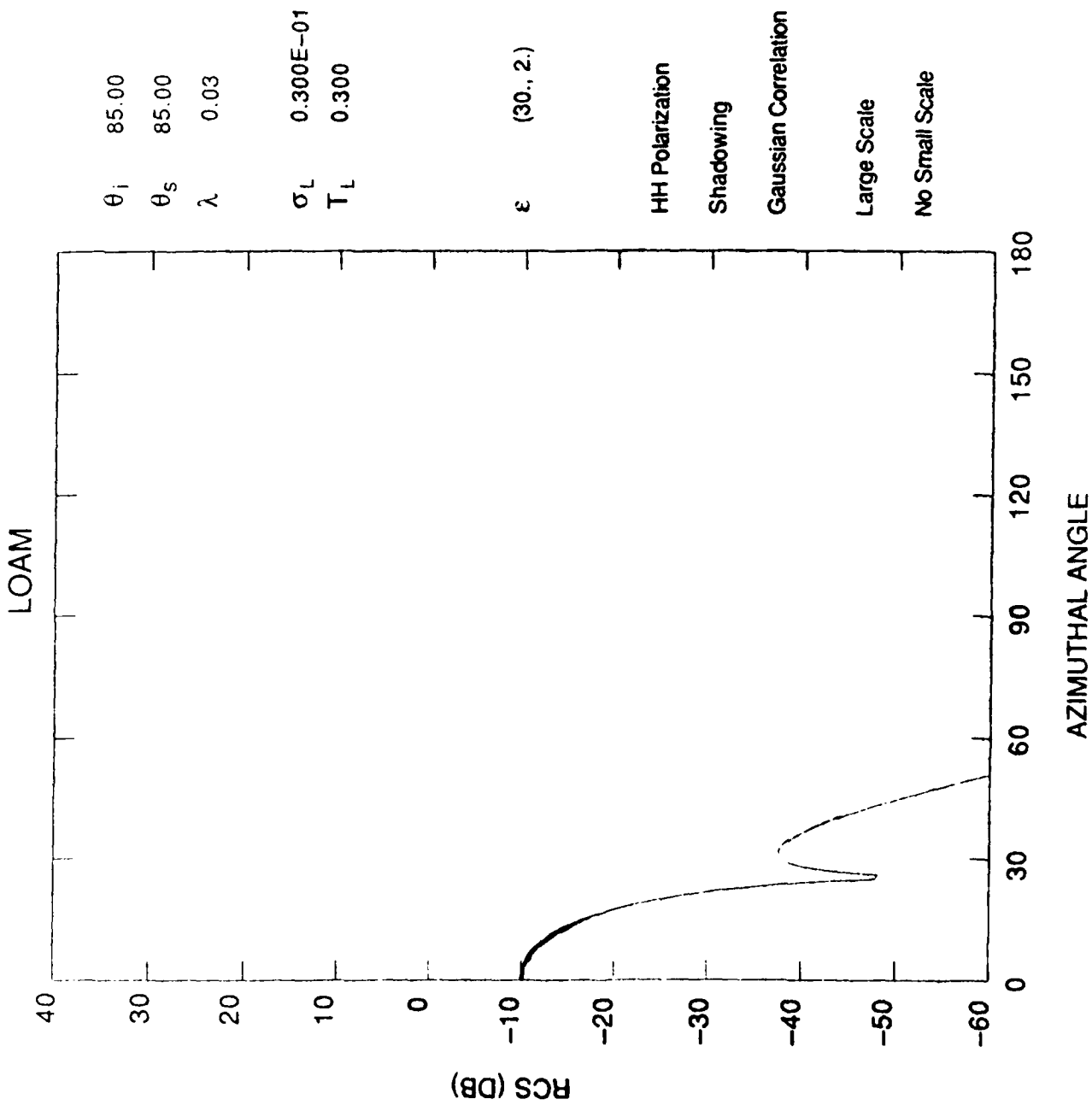


Figure 17. RCS vs. ϕ_s for Loam

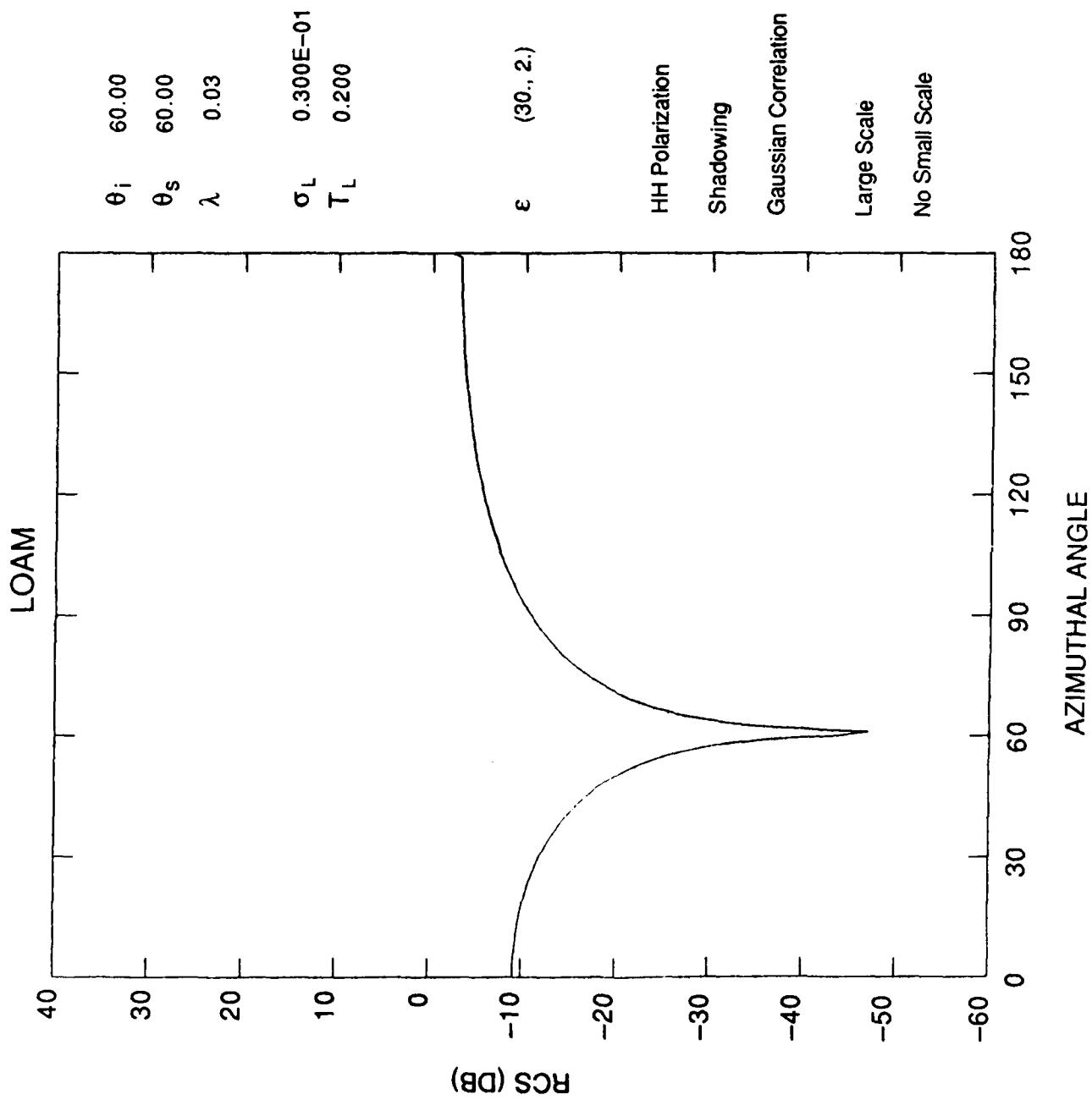


Figure 18. RCS vs. ϕ_s for Loam

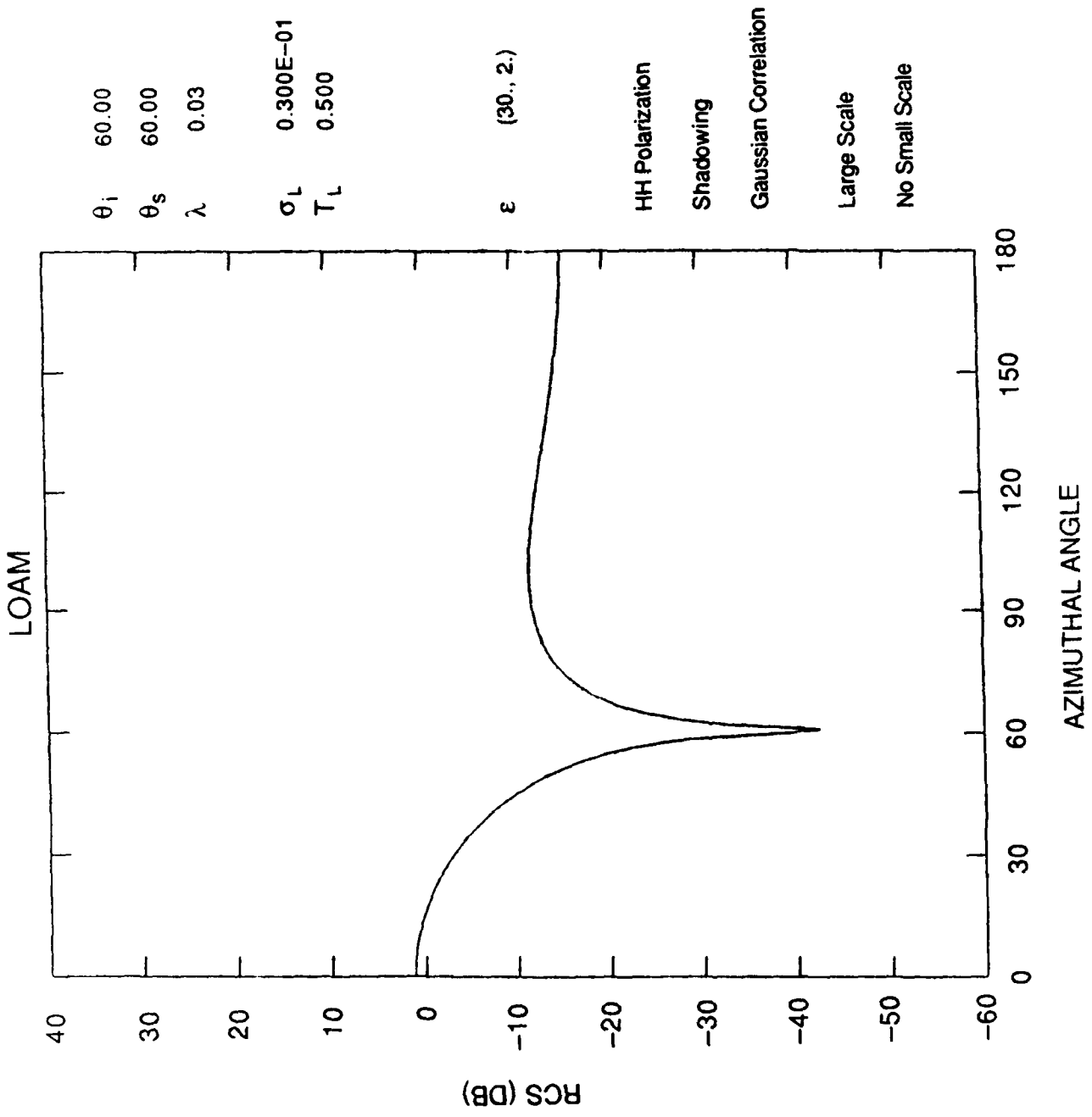


Figure 19. RCS vs. ϕ_s for Loam

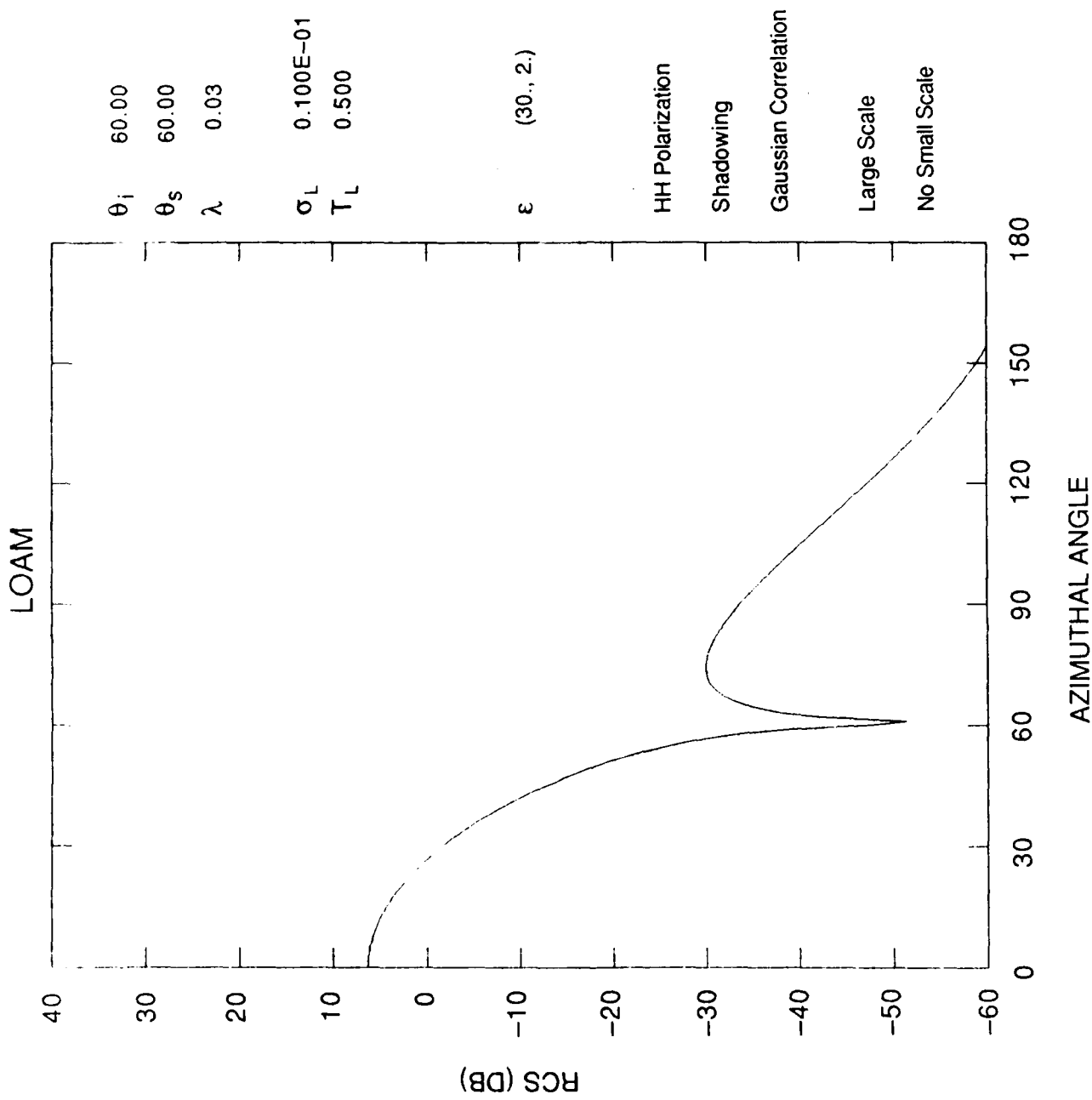


Figure 20. RCS vs. ϕ_s for Loam

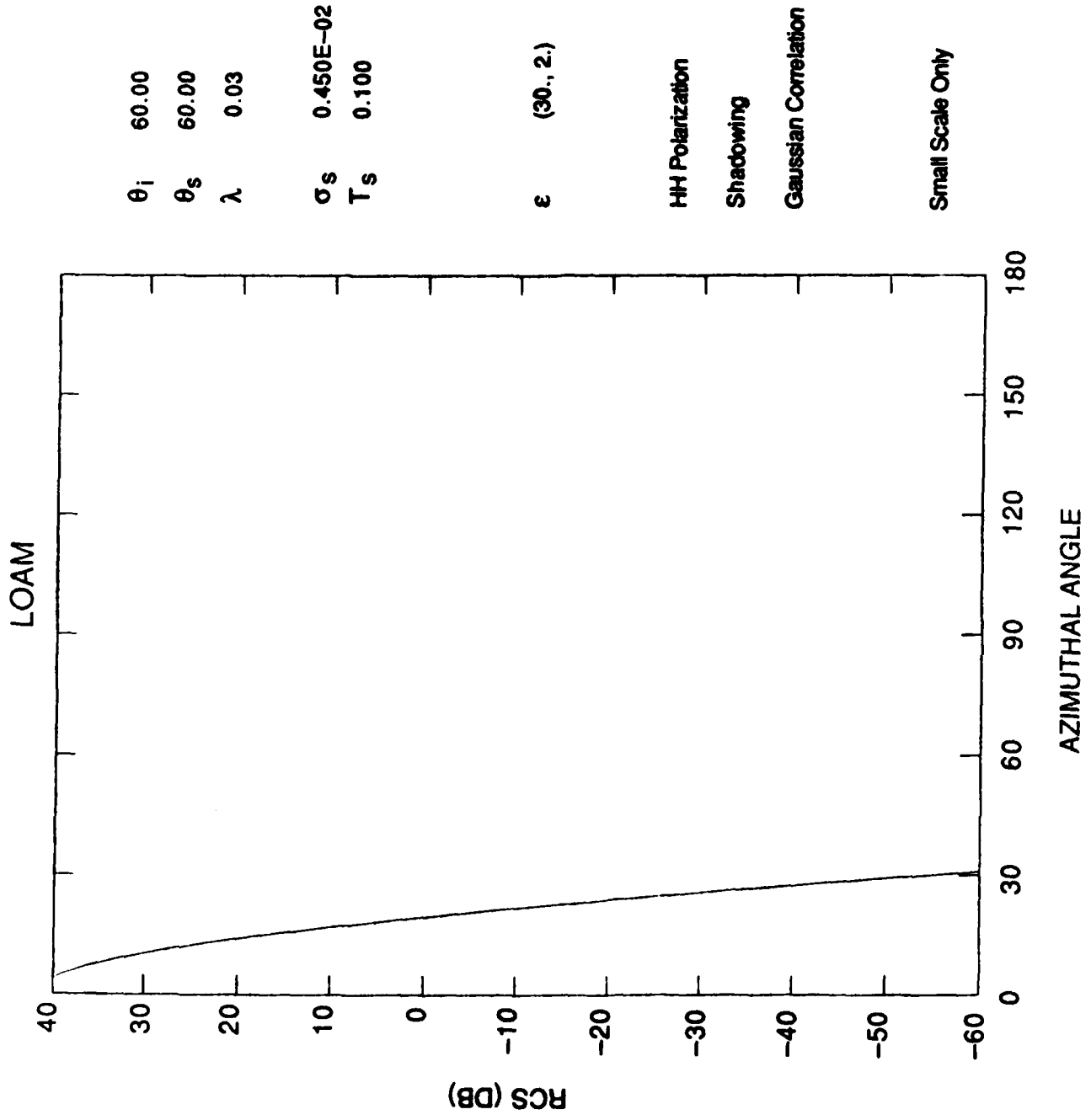


Figure 21. RCS vs. ϕ_s for LOAM

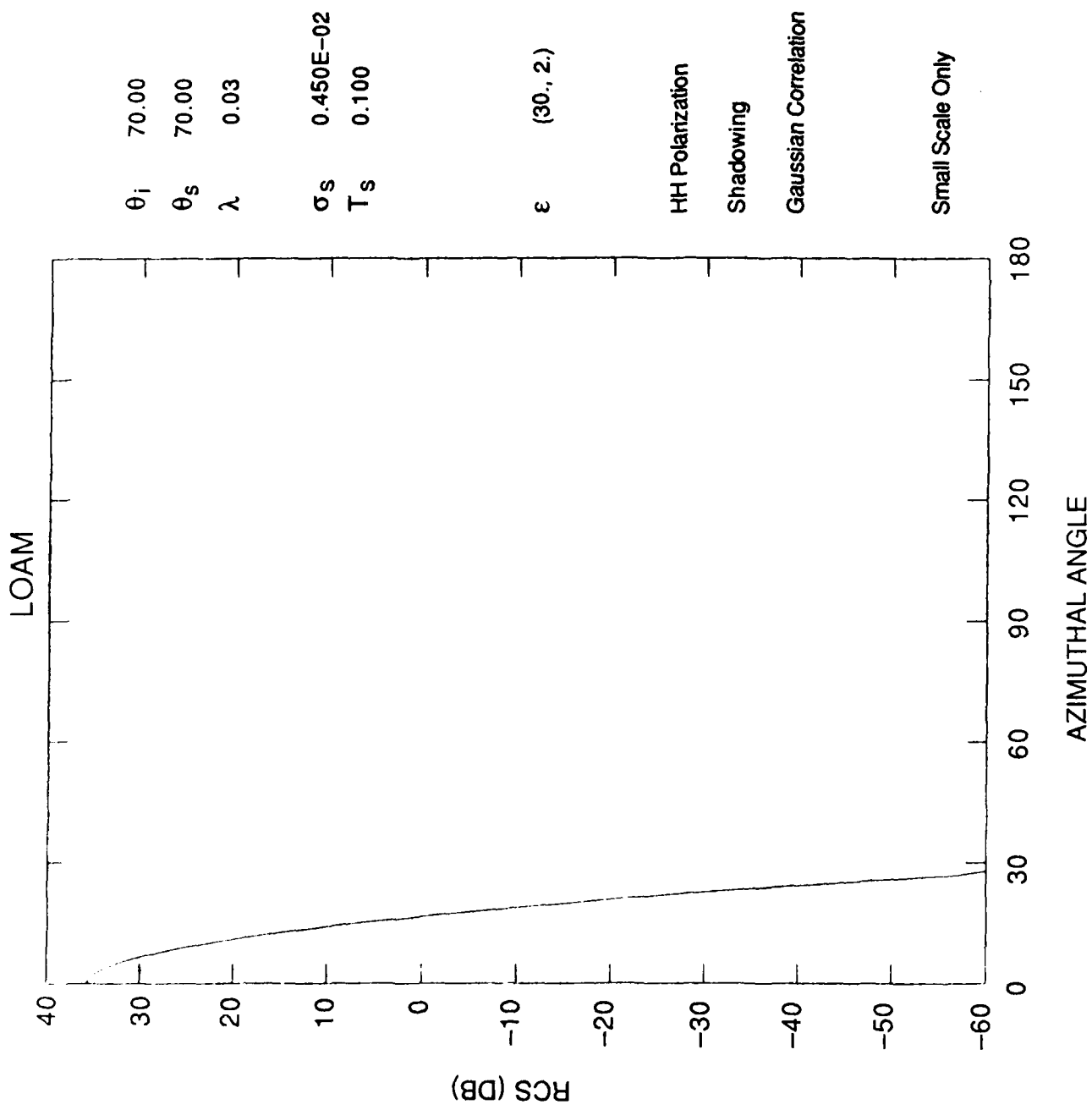


Figure 22. RCS vs. ϕ_s for Loam

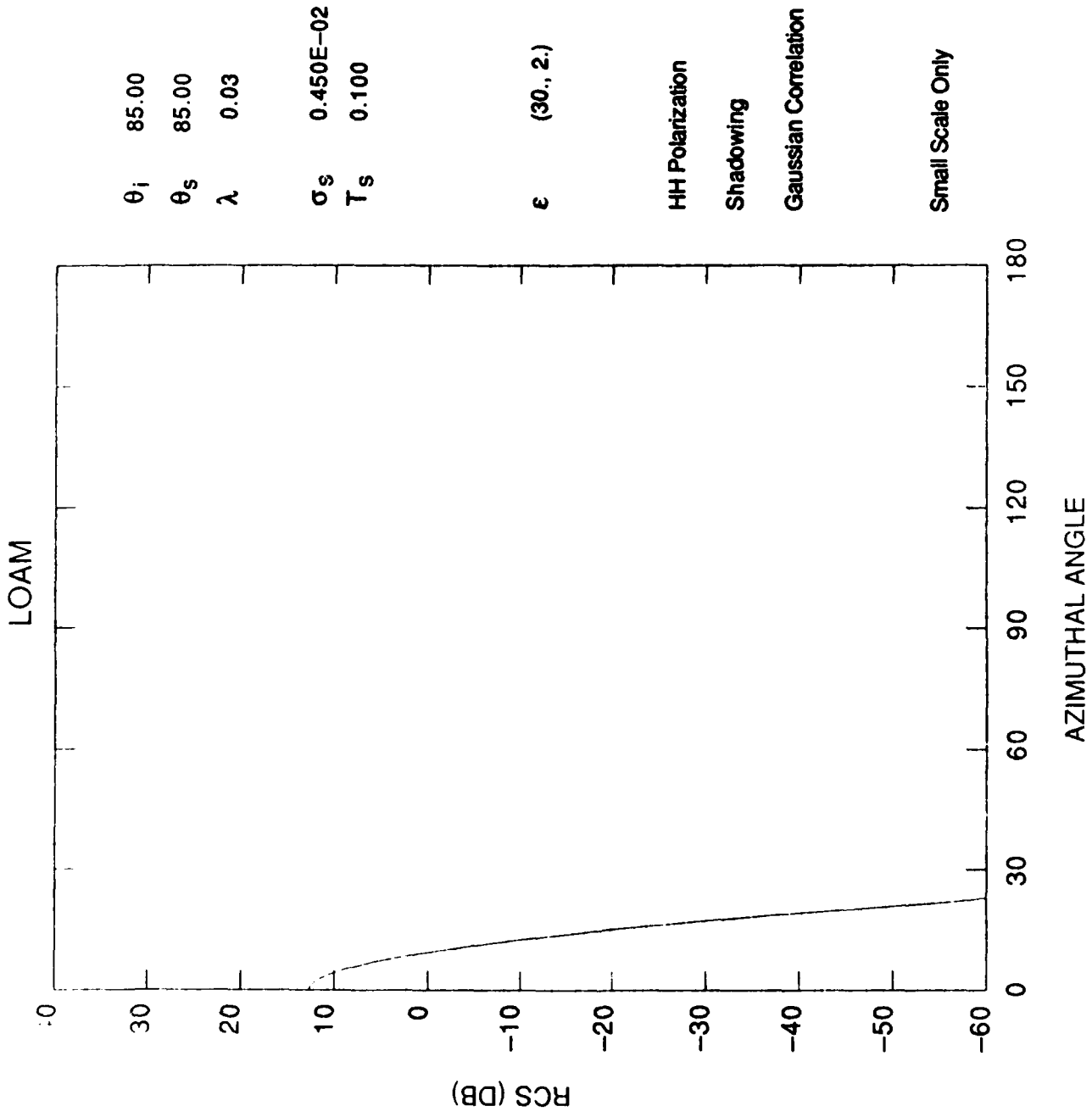
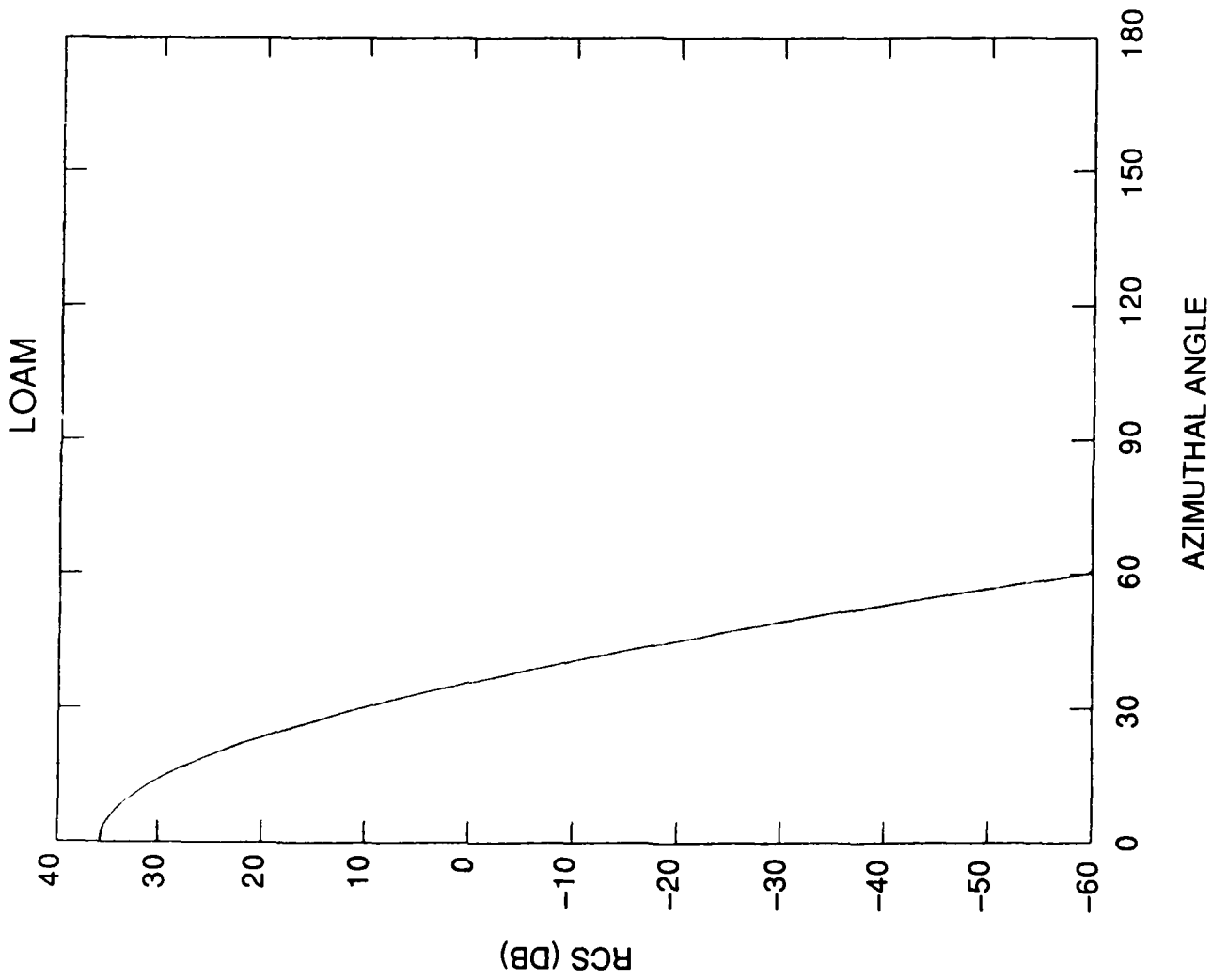


Figure 23. RCS vs. ϕ_s for LOAM



θ_i	60.00
θ_s	60.00
λ	0.03
σ_s	0.450E-02
T_s	0.500E-01
ϵ	(30., 2.)
	HH Polarization
	Shadowing
	Gaussian Correlation
	Small Scale Only

Figure 24. RCS vs. ϕ_s for Loam

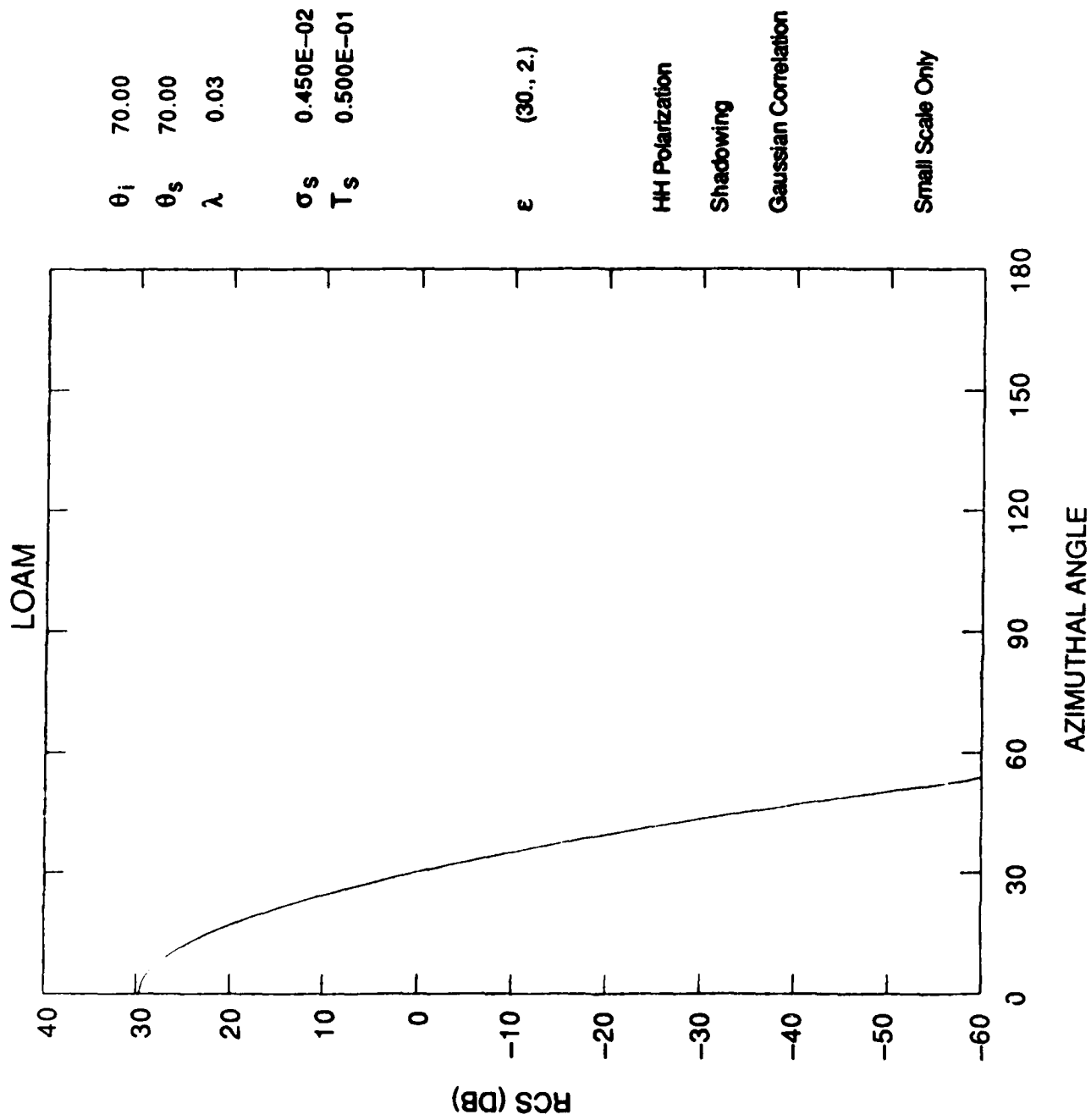
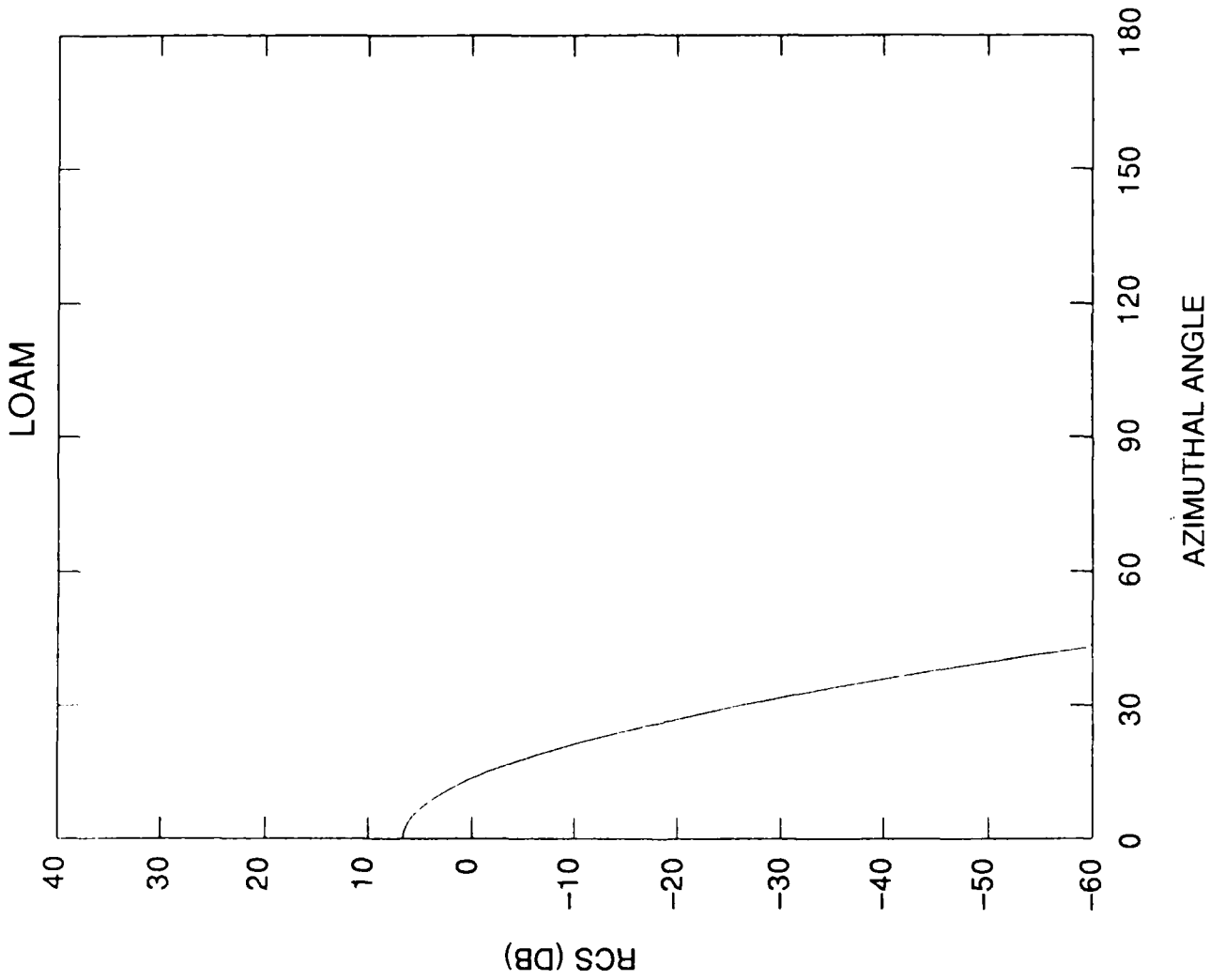


Figure 25. RCS vs. ϕ_s for Loam



θ_i 85.00
 θ_s 85.00
 λ 0.03
 σ_s 0.450E-02
 T_s 0.500E-01
 ϵ (30., 2.)
 HH Polarization
 Shadowing
 Gaussian Correlation
 Small Scale Only

Figure 26. RCS vs. ϕ_s for Loam

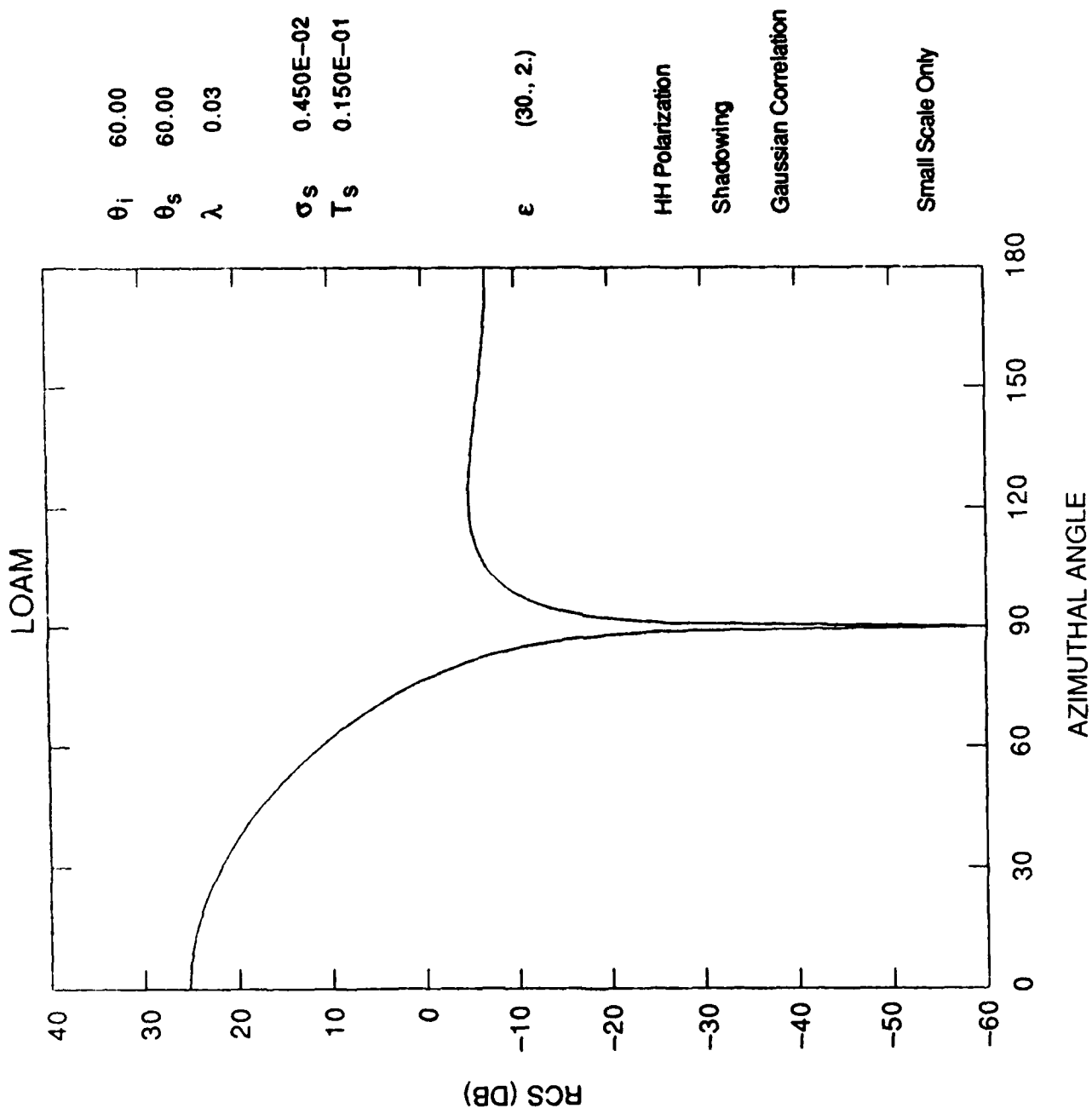


Figure 27. RCS vs. ϕ_s for Loam

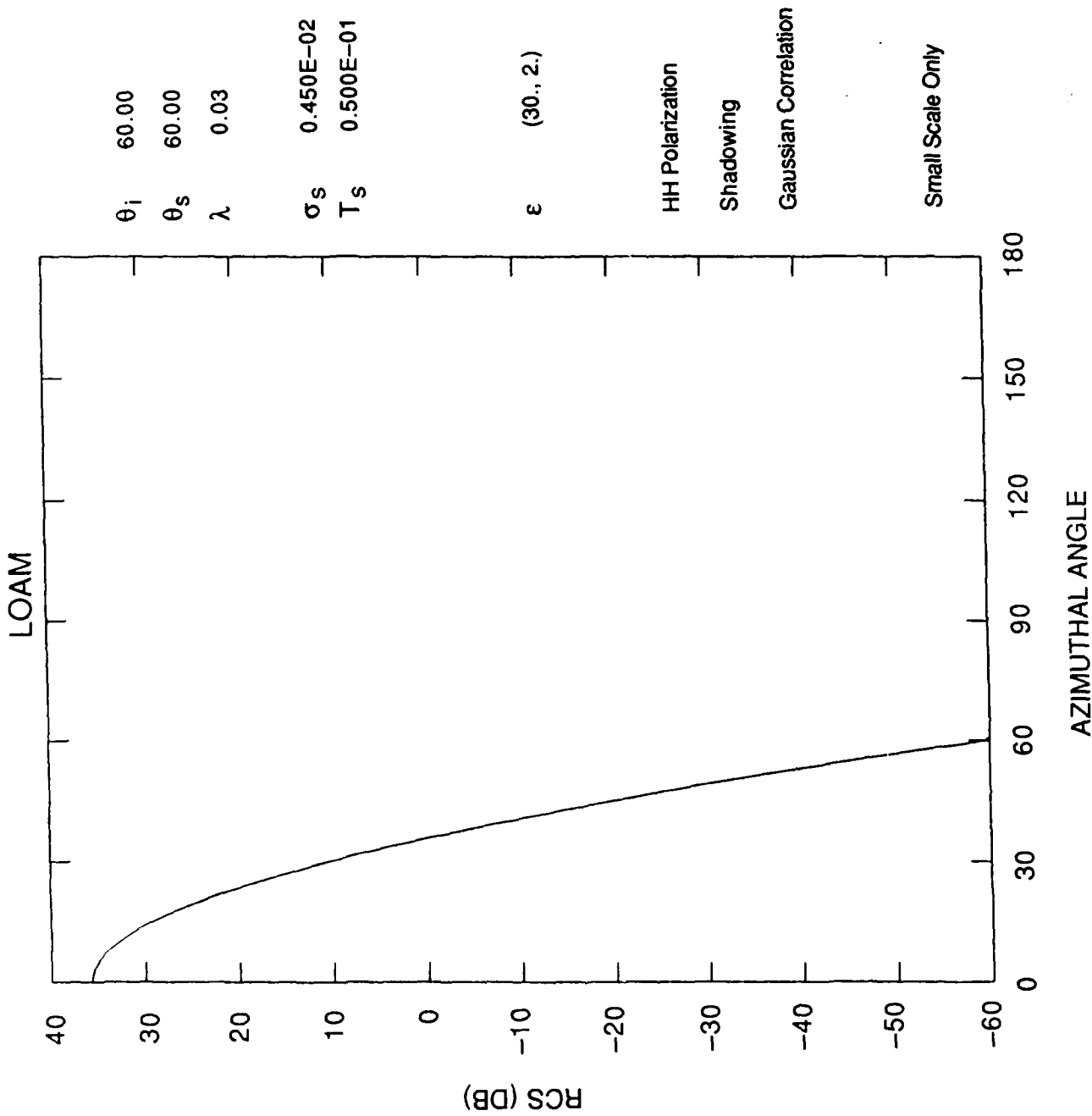


Figure 28. RCS vs. ϕ_s for Loam

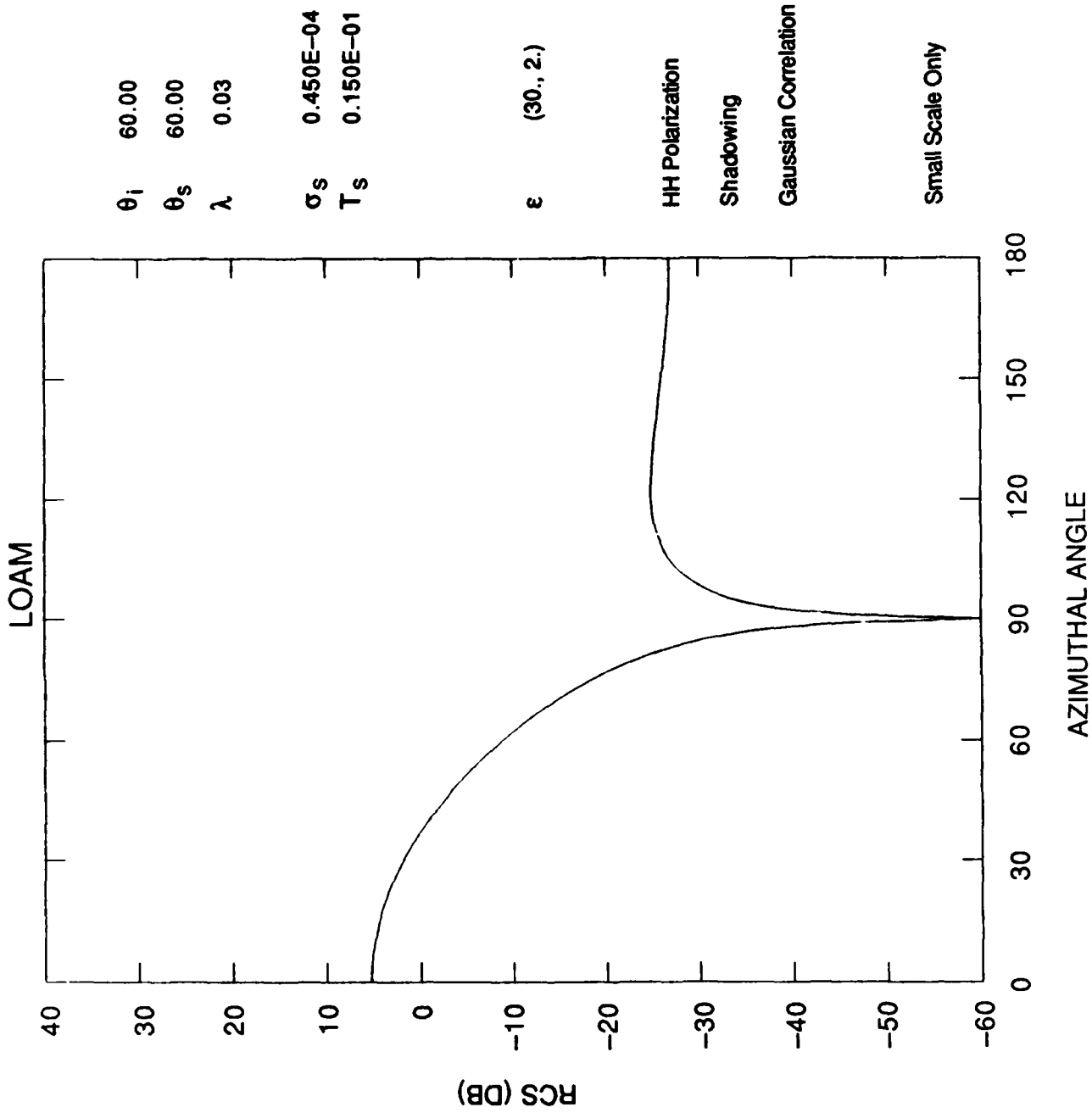


Figure 29. RCS vs. ϕ_s for Loam

Figures 27, 28, and 29 summarize the effects of the small scale roughness on the σ° vs. ϕ_s curves. Comparing Figure 28 with Figure 27, one may note a general trend; as T_s increases, the right hand side (backscatter) decreases and the left hand side (forward scatter) increases and the entire angular extent where σ° contributes becomes narrower (for σ_s constant, both HH and VV polarizations). Thus, T_s controls the shape of the σ° vs. ϕ_s curve. Comparing Figure 29 with Figure 27, one may note that as σ_s decreases, the entire σ° vs. ϕ_s curve moves down (decreases) and does not change shape (for T_s constant, both HH and VV polarizations).

4. BISTATIC AND MONOSTATIC CLUTTER MAPS

One question of interest is how the clutter cross section map of a region would change if a bistatic map were considered instead of a monostatic one. We will use our validated bistatic σ° model to demonstrate the differences for a particular scattering configuration. The region will consist of a loam surface extending some 200 nmi down range and 400 nmi cross range. A monostatic system is assumed to be at a grazing angle of about 6° with the front center of the region and about 2° with the rear. (The grazing angle is the complement of θ_i). These conditions apply to the scattered elevation angle values of the bistatic system. The bistatic incident elevation angle is taken with respect to the center of the region, $\theta_i = 70^\circ$. For both cases the σ° maps are constructed by dividing the region into 5 nmi by 5 nmi boxes and assigning a σ° value to the center of each box. Since the region is so extensive, the further refinement of a spherical geometry was introduced. The four-thirds earth radius concept then takes into account tropospheric refraction effects.

For this section the frequency is considered to be L-band ($f = 1$ GHz). The terrain is considered to be very rough but the constraint $\sigma_L/T_L < 1$ is maintained. Here $\sigma_L = 1.0$ m; $T_L = 1.1$ m; $\sigma_s = 0.0045$ m, $T_s = 1$ m; and $\epsilon = 30.0 + j 2.0$.

In Figure 30, the bistatic clutter map for loam is shown for horizontal-horizontal polarization, with the wavelength equal to 30 cm. The first observation to be noted is that the clutter cross section σ° is, in general, greatest in the direct forward, near specular, direction. This is due to the scattering in the forward, near specular direction (small slopes, $\sigma_L/T_L < 1$). The decrease in clutter cross section σ° with increasing range is due primarily to shadowing. The surface irregularities cause less of the rough surface to be illuminated by the incident rays as the elevation scattering angle θ_s decreases.

In Figure 31, the monostatic clutter map for loam is shown for horizontal-horizontal polarization. It may be noted immediately that, for a given clutter cell, the monostatic cross section σ° is, in general, at least 50 dB less than the corresponding bistatic cross section. Since the monostatic cross section σ° has a fixed azimuthal scattering angle ($\phi_s = 180^\circ$), the monostatic clutter map is circularly symmetric about the radar position. The behavior of the monostatic cross section σ° with range is similar to the bistatic cross section; σ° decreases as the range increases primarily because of shadowing.

Figure 32 is not a clutter map, rather, it is a clutter ratio map, that is, σ°_{HH} (monostatic)/ σ°_{HH} (bistatic). It may be noted immediately from Figure 32 that for any cell, the monostatic cross section is at least 50 dB less than the corresponding bistatic cross section σ° .

Figure 33 is a bistatic clutter map for loam for vertical-vertical polarization. Comparing Figure 33 with Figure 30 shows that in the forward scatter direction, the bistatic cross section σ°_{VV} is

BISTATIC CLUTTER

LOAM HH POLARIZATION GAUSSIAN CORRELATION FUNCTION

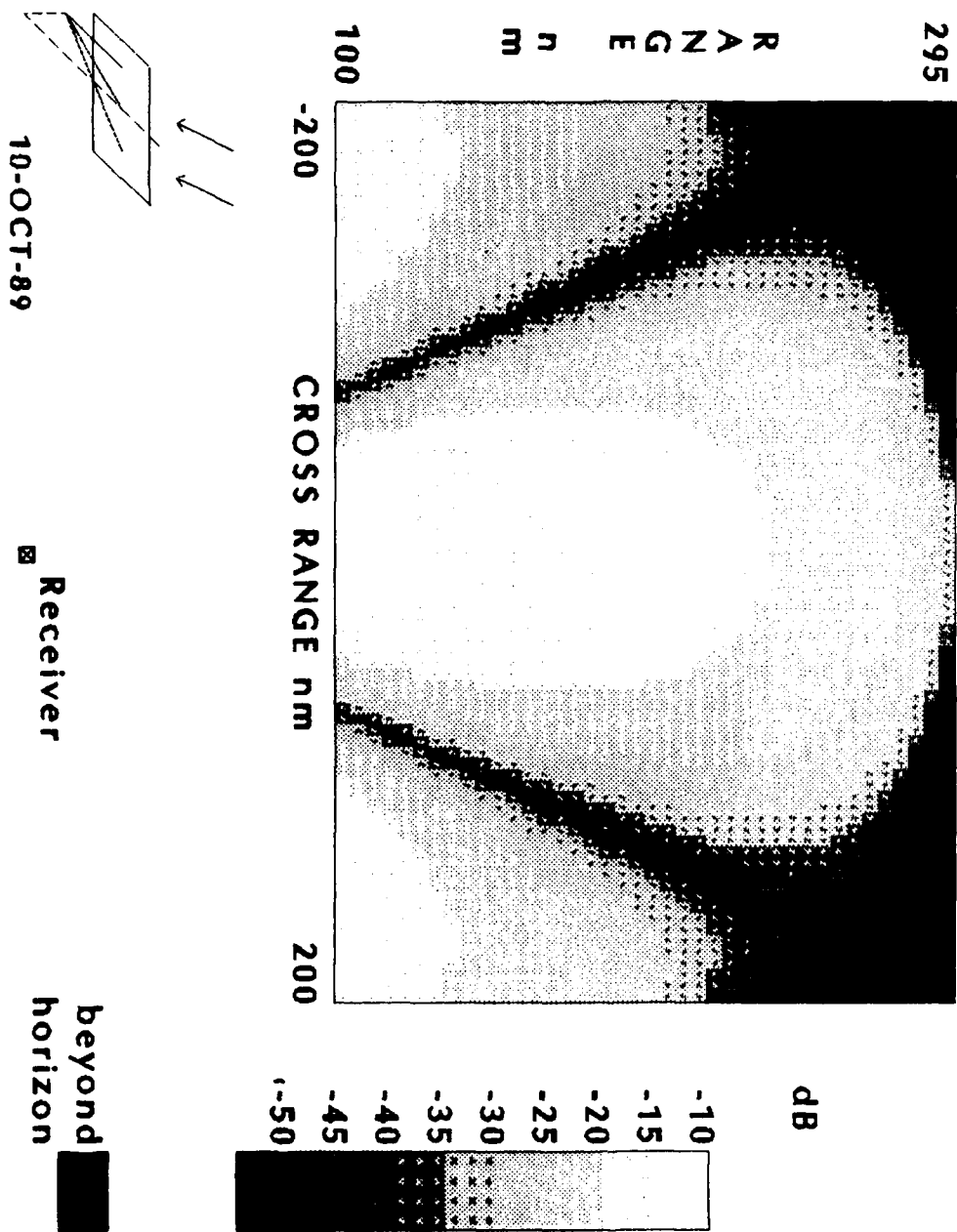


Figure 30. Bistatic Clutter Map for Loam (HH Polarization)

MONOSTATIC CLUTTER

LOAM HH POLARIZATION GAUSSIAN CORRELATION FUNCTION

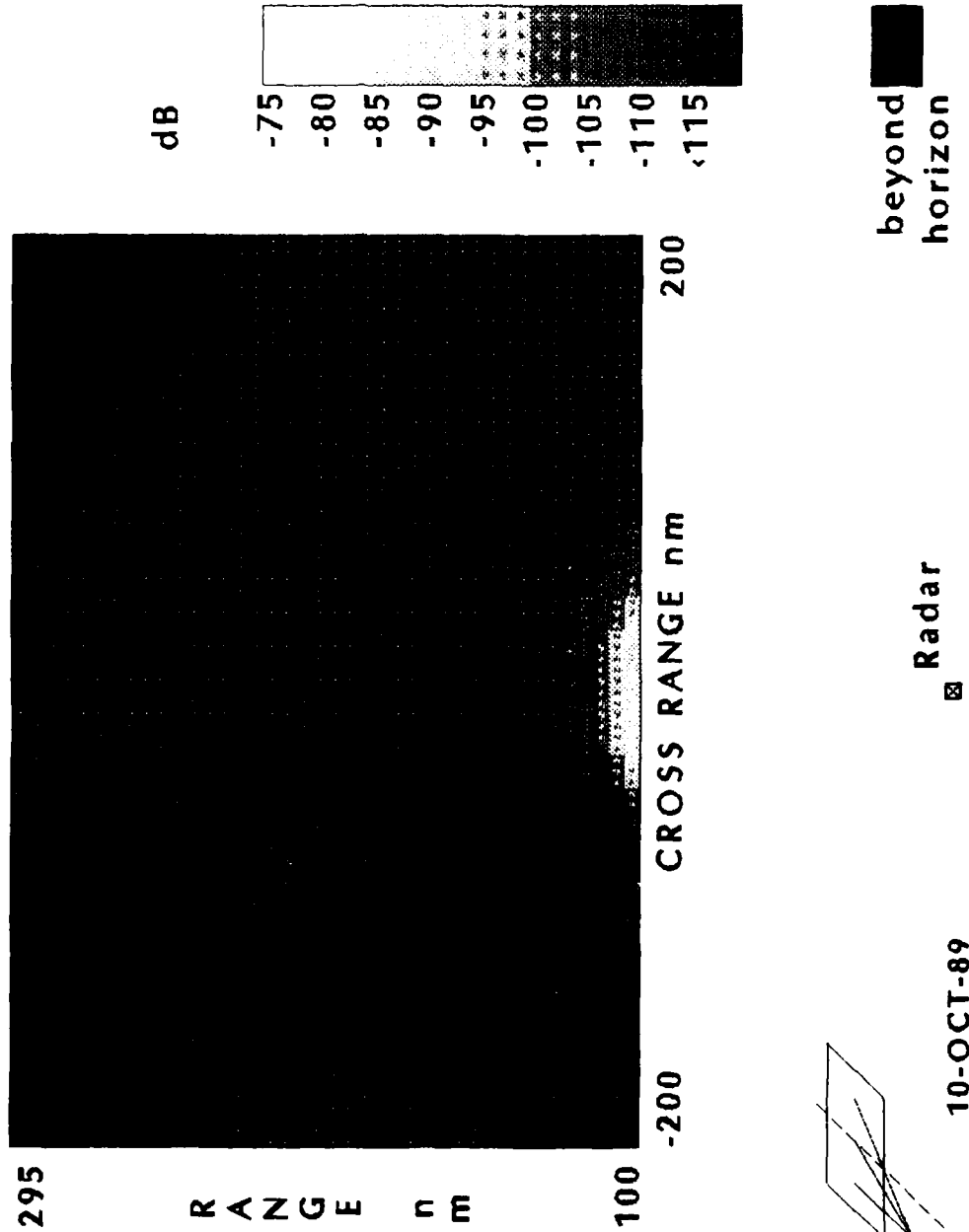


Figure 31. Monostatic Clutter Map for Loam (HH Polarization)

MONOSTATIC/BISTATIC RATIO

LOAM HH POLARIZATION GAUSSIAN CORRELATION FUNCTION

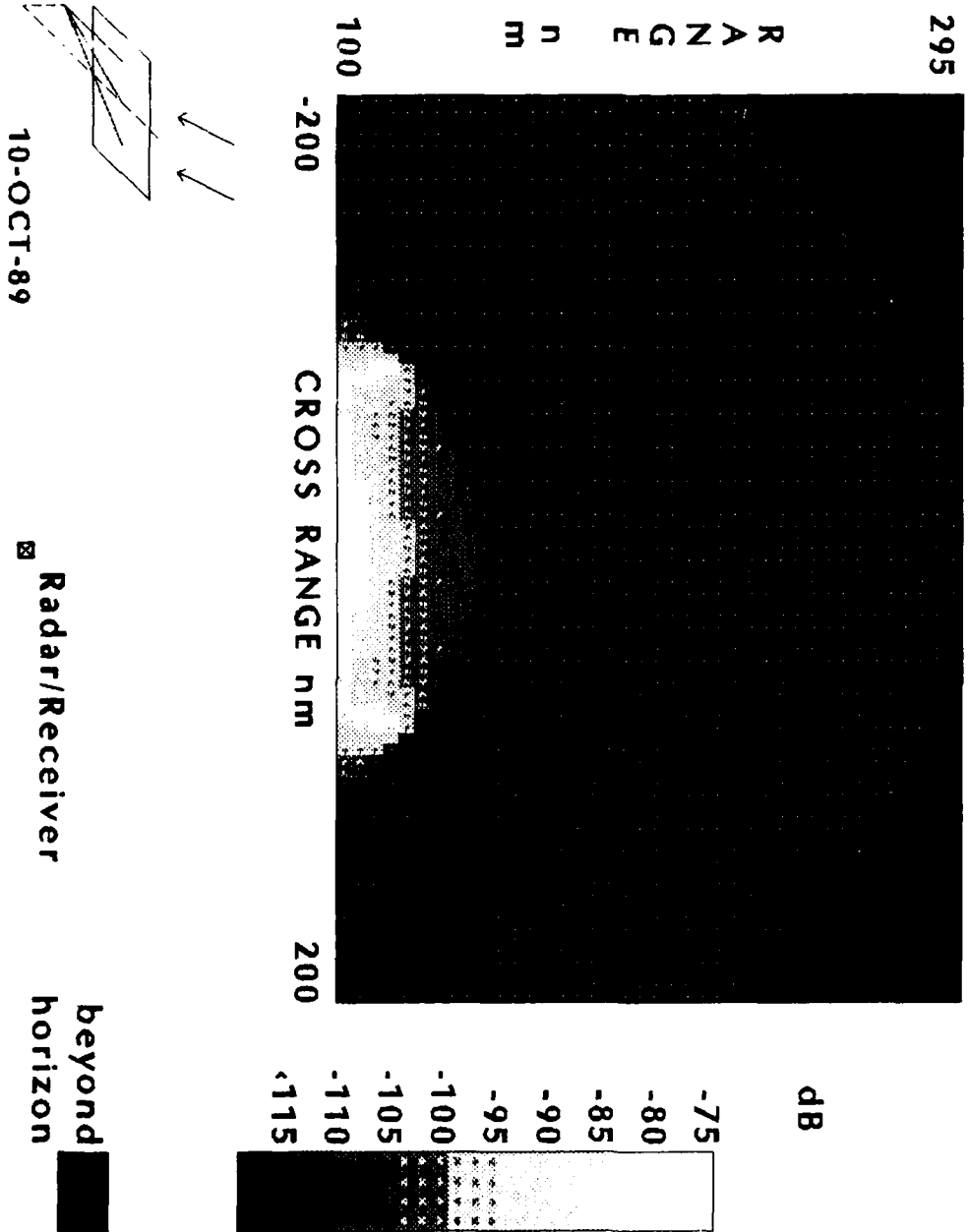


Figure 32. Monostatic/Bistatic Ratio Map for Loam (HH Polarization)

BISTATIC CLUTTER

LOAM VV POLARIZATION GAUSSIAN CORRELATION FUNCTION

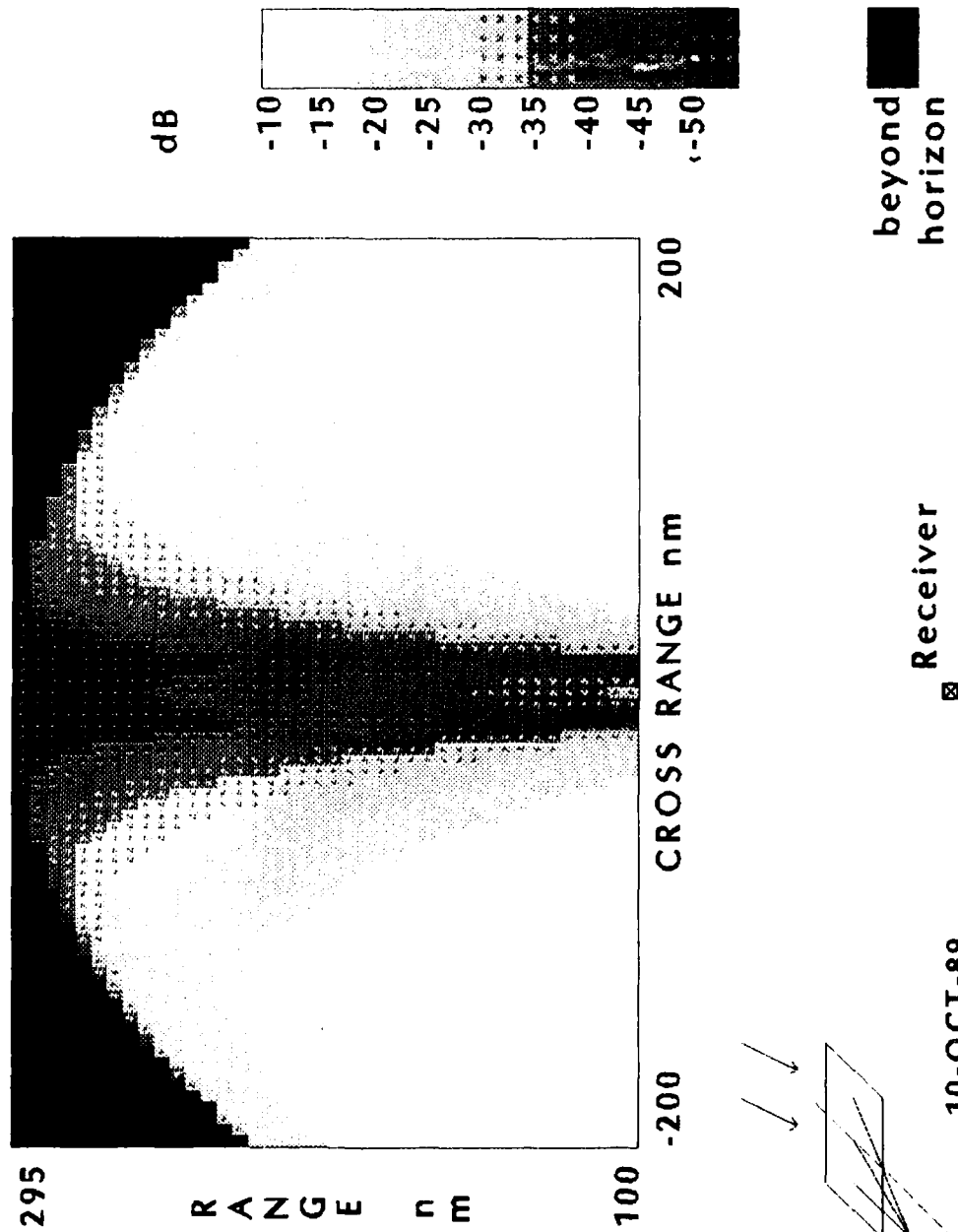


Figure 33. Bistatic Clutter Map for Loam (VV Polarization)

about 20 dB less than σ_{HH}° . For larger azimuthal scattering angles, corresponding to a cross range > 50 nmi, the bistatic cross section σ_{VV}° is, in general, greater than σ_{HH}° . The behavior of σ_{VV}° with range is similar to σ_{HH}° ; it decreases as the range increases because of shadowing.

Figure 34 is a monostatic clutter map for loam for vertical-vertical polarization. Comparing Figure 34 with Figure 31, we may note that the monostatic cross section σ_{VV}° for a given clutter cell is very nearly identical to σ_{HH}° .

Figure 35 is a map of the ratio σ_{VV}° (monostatic)/ σ_{VV}° (bistatic). It may be noted immediately that the monostatic cross section σ_{VV}° is at least 45 dB less than the bistatic σ_{VV}° for any given clutter cell. Comparing Figure 35 with Figure 32, it may be noted that the two map ratios σ° (monostatic)/ σ° (bistatic) for the two polarizations are quite distinct. This is due primarily to the differences in the two bistatic cross sections.

5. CONCLUSIONS

Reasonable agreement was obtained between the bistatic scattering model with two scales of roughness and the X-band data.² Both elevation plane comparisons for sand and azimuthal results for loam were considered. Considering the sparseness of the data and the limited nature of the ground truth, it appears that sufficient accuracy and trend preservation can be obtained using the theoretical model. It should be noted that, where the agreement is poorest (small incident grazing angle), both the data and the model are suspect. The uncertainty in the data is caused by the footprint determination requirement while the physical optics model does not allow multiple scattering which is more likely to occur at those conditions.

The parametric studies in which each level of roughness was treated separately allowed us to evaluate the model performance. The physical optics terms were dominant in the forward scattering directions and in those cases the results were controlled by the surface slope. As the scattering extended beyond these regions, the physical optics results were not as significant and the behavior was no longer slope dependent. Different patterns occurred depending on whether the standard deviation in heights or the correlation length was varied. The perturbation theory (small scale) results do not show any direct slope related pattern. For all cases there is a distinct difference in behavior to the curves when either σ_s or T_s is varied. σ_s affects the magnitude and T_s affects the shape of the small scale pattern.

When the validated bistatic scattering model was used to compare bistatic and monostatic clutter cross sections for a loam covered surface subdivided into 5 nmi boxes the results showed that the bistatic σ° values for the configuration used in the analysis always exceed the corresponding monostatic values by 50 dB for horizontal polarization and by 45 dB for vertical polarization. Shadowing, as expected, played a more significant role for the furthest down range cells. For this type of geometry, any enhanced target detection using bistatics has to come from greatly increased target cross sections at bistatic angles.

MONOSTATIC CLUTTER

LOAM VV POLARIZATION GAUSSIAN CORRELATION FUNCTION

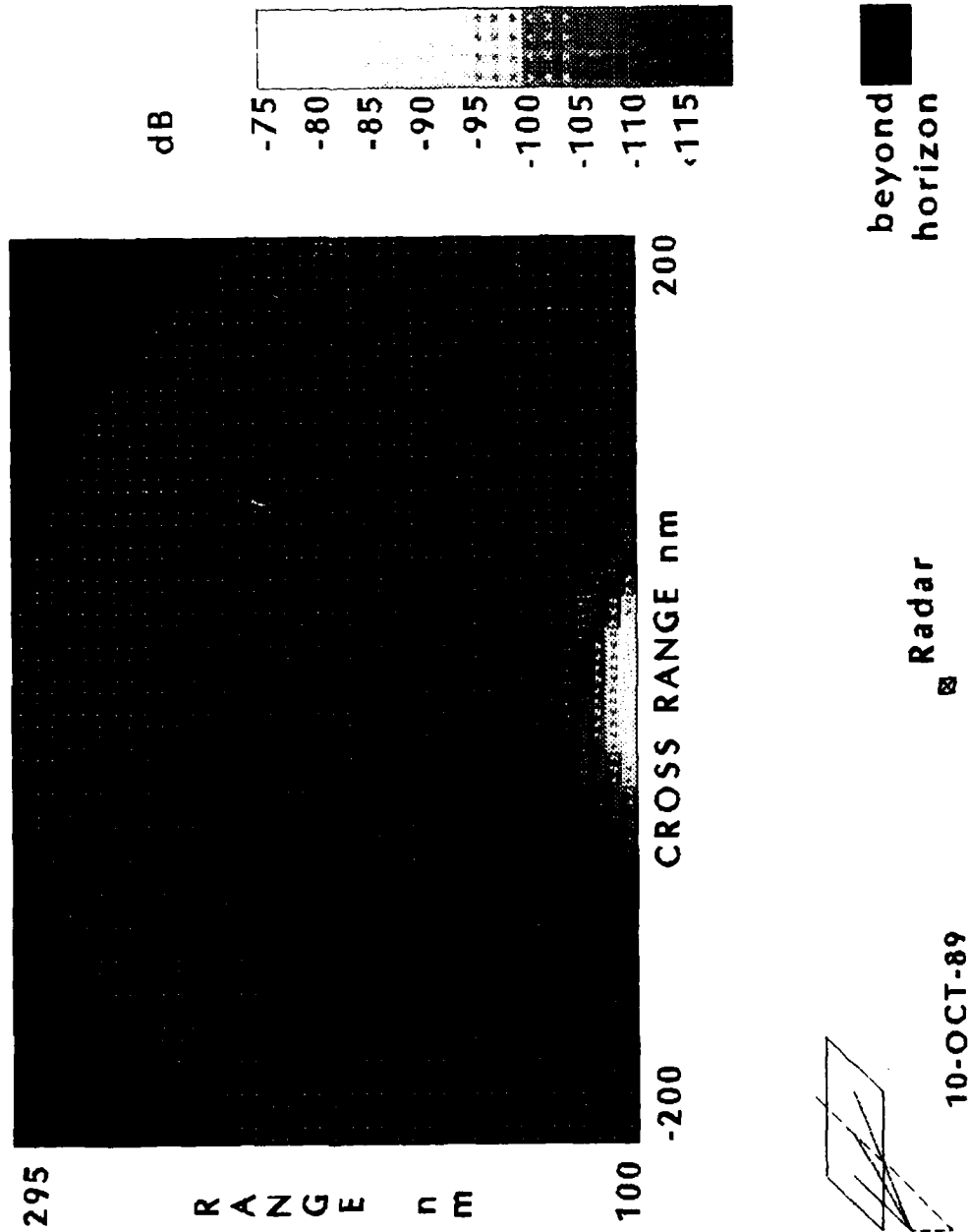


Figure 34. Monostatic Clutter Map for Loam (VV Polarization)

MONOSTATIC/BISTATIC RATIO

LOAM VV POLARIZATION GAUSSIAN CORRELATION FUNCTION

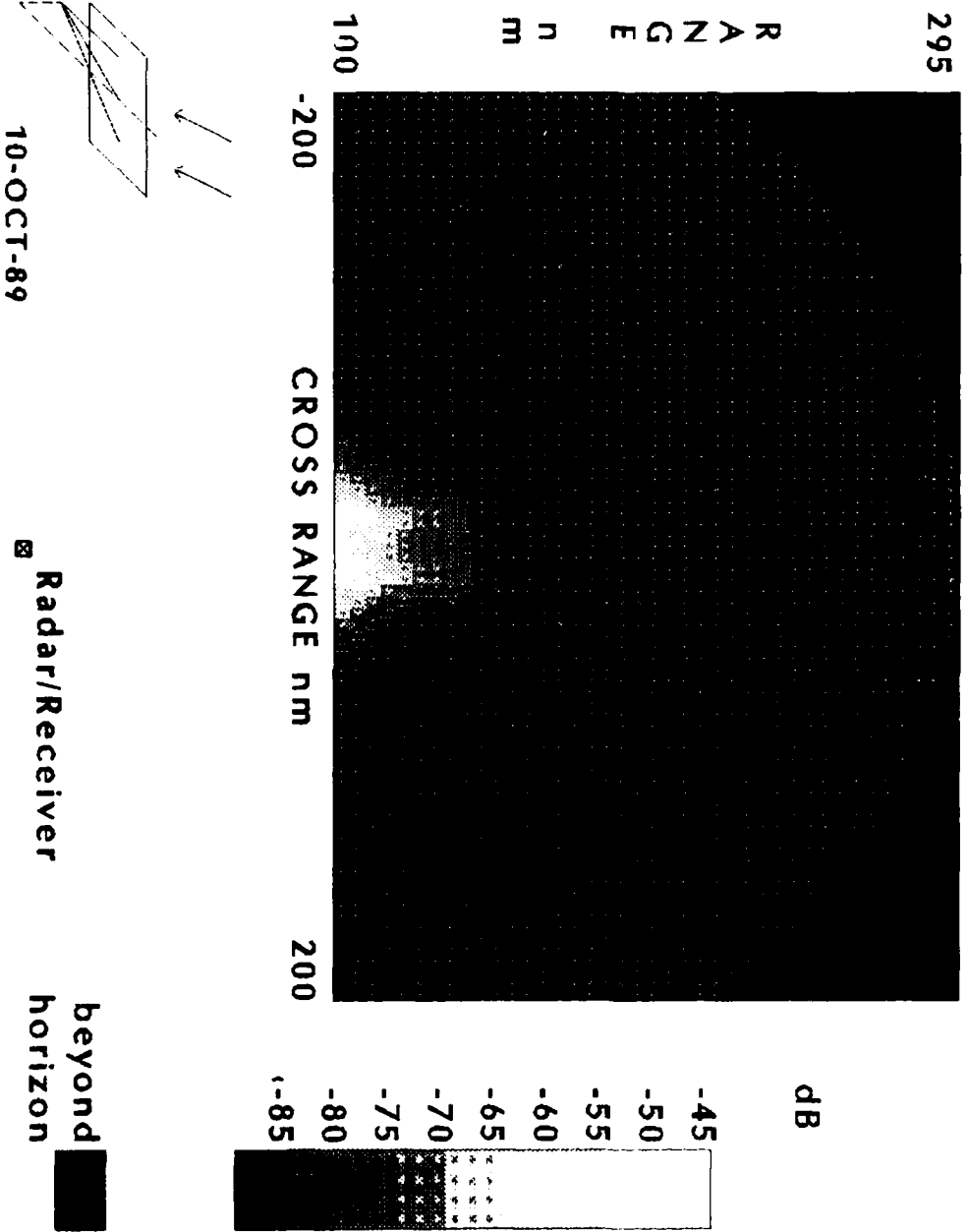


Figure 35. Monostatic/Bistatic Ratio Map for Loam (VV Polarization)

References

1. Ruck, G.T., Barrick, D.E., Stuart, W.D., and Krichbaum, C.K. (1970) *Radar Cross Section Handbook*, Vol. 2, Plenum Press, New York.
2. Cost, S.T. (1965) *Measurements of the Bistatic Echo Area of Terrain at X-band*, Master's Thesis, Ohio State University.
3. Papa, R.J., Lennon, J.F., and Taylor, R.L. (1984) *An Analysis of Physical Optics Models for Rough Surface Scattering*, RADC-TR-84-195, ADA 154960.
4. Brown, G.S. (1978) Backscattering from a Gaussian distributed, perfectly conducting, rough surface, *IEEE Trans. Antennas Propag.* **AP-26**:472-482.
5. Sancer, M.I. (1969) Shadow corrected electromagnetic scattering from a randomly rough surface, *IEEE Trans. Antennas Propag.* **AP-17**:577-585.



MISSION
of
Rome Air Development Center

RADC plans and executes research, development, test and selected acquisition programs in support of Command, Control, Communications and Intelligence (C³I) activities. Technical and engineering support within areas of competence is provided to ESD Program Offices (POs) and other ESD elements to perform effective acquisition of C³I systems. The areas of technical competence include communications, command and control, battle management, information processing, surveillance sensors, intelligence data collection and handling, solid state sciences, electromagnetics, and propagation, and electronic, maintainability, and compatibility.